Connecting macroscopic diffusion metrics of cardiac diffusion tensor imaging and microscopic myocardial structures based on simulation

Lihui Wang, Yao Hong, Yong-Bin Qin, Xin-Yu Cheng, Feng Yang, Jie Yang, Yue-Min Zhu

Medical Image Analysis (2021)

Contents lists available at ScienceDirect

Medical Image Analysis

journal homepage: www.elsevier.com/locate/media

Connecting macroscopic diffusion metrics of cardiac diffusion tensor imaging and microscopic myocardial structures based on simulation

Lihui WANG[a], Yao HONG[a], Yong-Bin QIN[a,*], Xin-Yu CHENG[a], Feng YANG[b], Jie YANG[c], Yue-Min ZHU[d]

[a]*Key Laboratory of Intelligent Medical Image Analysis and Precise Diagnosis of Guizhou Province, College of Computer Science and Technology, Guizhou University, Guiyang 550025, China*
[b]*School of Computer and Information Technology, Beijing Jiaotong University, Beijing 100044, China*
[c]*Institute of Image Processing and Pattern Recognition, Shanghai Jiao Tong University, Shanghai 200240, China*
[d]*University Lyon, INSA Lyon, CNRS, Inserm, IRP Metislab CREATIS UMR5220, U1206, Lyon 69621, France*

ARTICLE INFO

Article history:
Received 27 Oct 2019
Received in final form xx xx 2019
Accepted xx xx 2019
Available online xx xx 2020

Keywords: Bloch equation, Brownian motion, DTI, Myocardium, Polarized light imaging

ABSTRACT

To investigate the relationship between microscopic myocardial structures and macroscopic measurements of diffusion tensor imaging (DTI), we propose a cardiac DTI simulation method using Bloch equation and Monte Carlo random walking in a realistic myocardium model reconstructed from polarized light imaging (PLI) data of whole human hearts. To get a realistic simulation, with the constraints of prior knowledge about the maturational change of myocardium structure, appropriate microstructure modeling parameters are iteratively determined by matching DTI simulations and real acquisitions of the same hearts in terms of helix angle, fractional anisotropy (FA) and mean diffusivity (MD) maps. Once the realistic simulation was obtained, we varied extracellular volume (ECV) ratio, myocyte orientation heterogeneity and myocyte size, and explored the effects of microscopic tissue structure change on macroscopic diffusion metrics. The experimental results demonstrated the feasibility of simulating DTI of a whole heart using PLI measurements. When varying ECV from 15% to 55%, mean FA decreased from 0.55 to 0.26, axial diffusivity increased by 0.6 $\mu m^2/ms$, and radial diffusivity increased by 0.7 $\mu m^2/ms$. Mean FA decreased from 0.4 to 0.3, and axial diffusivity decreased by 0.08 $\mu m^2/ms$ but radial diffusivity increased by 0.03 $\mu m^2/ms$, when orientation heterogeneity was varied from 0 to 20°. When mean diameter of myocytes was varied from 6 μm to 10 μm, FA decreased from 0.67 to 0.46, and axial and radial diffusivities increased by respectively 0.05 and 0.2 $\mu m^2/ms$.

1. Introduction

The myocardium is crucial to maintaining normal cardiac functions. It has been demonstrated that the myocardium's individual cardiac myocytes, which are connected by intercalated discs and form a sort of cardiac fibers, allow for the propagation of electrical impulses (Rohr, 2004; McCain et al., 2014) and that the electrical propagation is faster along the myocyte orientation than along

*Corresponding author: Tel.: +0-08618085008039;
e-mail: {ybqin@foxmail.com},{lhwang2@gzu.edu.cn} (Yong-Bin QIN)

its sheetlet plane (Benson et al., 2011). The fibrous extra-cellular matrix responses to mechanical strain (Spach et al., 1998) and cardiac contractions are mainly explained by the myocyte arrangement (Eriksson et al., 2013). Therefore, investigating myocardial fiber architecture is one of the most important means to explore the physiological and pathological properties of the heart (Helm et al., 2006).

Early descriptions of myocardial fiber architecture were derived from histological measurements (Scollan et al., 1998). However, such measurements require a long reconstruction time and suffer from myocardium distortion during tissue preparation; therefore, they cannot provide an accurate description of the whole myocardium architecture for a large number of hearts. A more accurate description of the myocardium structure using polarized light imaging (PLI) was proposed (Jouk et al., 1995, 2007; Desrosiers et al., 2016), which can provide a three-dimensional (3D) description of an whole heart with a high spatial resolution through physical measurements. PLI can thus offer the ground truth for investigating the myocardium structure (Yang et al., 2018). However, fiber orientations alone are not enough for obtaining a complete description of myocardium; other parameters are needed to reflect the variation of myocardial fiber structures. Recently, diffusion tensor imaging (DTI), which is a particular magnetic resonance imaging (MRI) technique, has appeared as a promising technique for non-invasively investigating the fiber architectures of both *ex vivo* (Hsu and Henriquez, 2001; Helm et al., 2005; Wu et al., 2007; Abdullah et al., 2016; Lombaert et al., 2012) and *in vivo* hearts (Toussaint et al., 2013; Ferreira et al., 2014; Axel et al., 2014; Welsh et al., 2015; Wei et al., 2015; Nguyen et al., 2016; Von Deuster et al., 2016; Moulin et al., 2016; Nielles-Vallespin et al., 2017; Khalique and Pennell, 2019). It enables us to infer not only cardiac fiber orientations but also other diffusion metrics such as diffusion anisotropy (FA) and mean diffusivity (MD) by detecting the displacement distribution of water molecules in the myocardium. By exploring the microscopic displacement of water molecules in tissues, DTI provides an effective way to probe the microstructure of tissues at the sub-voxel level, which makes it possible to investigate cardiac diseases that cause changes in myocardium tissue microstructure. For instance, it has been demonstrated that cardiac myocyte orientation was disarrayed in hypertrophic cardiomyopathy (Tseng et al., 2006; Ariga et al., 2019; Cook et al., 2019; Von Deuster et al., 2016) and that diffusion metrics of DTI such as FA and MD changed in myocardial infarction (Strijkers et al., 2009; Nguyen et al., 2018a). Although FA and MD can characterize some cardiac diseases, their variation could in fact be the consequence of a series of changes in microstructures. The relationship between myocardial microstructures and macroscopic measurements in DTI remains to be elucidated. A number of techniques have been proposed to probe tissue microscopic structures, such as DIAMOND (Scherrer et al., 2016), MAPL (Fick et al., 2016), AMICO (Daducci et al., 2015) and NODDI (Tariq et al., 2016). However, without the ground truth, these estimations derived from analytical models with assumptions need to be further evaluated.

To deal with this problem, numerous modeling and simulation methods have been proposed, which simulate diffusion signals by tracking the diffusion displacement of water molecules in a controlled geometric model (Wang et al., 2012; Ianuş et al., 2016; Gilani et al., 2017; Bates et al., 2017; Rensonnet et al., 2019; Brusini et al., 2019; Nguyen et al., 2018b; Sapkota et al., 2016; Lee et al., 2020a). Since the microstructure configuration is under control, numerical simulation provides a valuable tool to accurately investigate the relationship between macroscopic diffusion metrics and underlying microscopic structures. In recent years, several works have focused on the simulation of brain DTI. The software package Camino (Cook et al., 2006) has been used to simulate DTI of the brain with various geometrical models. Molecular motion simulation packages (Smoldyn (Andrews et al., 2010) or MCell (Kerr et al., 2008)) have been used to synthesize diffusion-weighted (DW) signals in complex environments. Specific simulators have also been considered to investigate the dependence of diffusion metrics on the microscopic structures of brain or muscle tissues (Yeh, 2011; Yeh et al., 2013; Berry et al., 2018; Lee et al., 2020c,d). However, most of these works dealt with the brain, except

the works of Bates (Bates et al., 2017) and Rose (Rose et al., 2019), which were dedicated to simulating cardiac DTI with much more realistic structures. Bates et al. first modeled the myocardium structure in a voxel with arranged cubics, then simulated the corresponding diffusion weighted signal, and finally validated their simulation using the acquired cardiac DTI. Such validation within a single voxel cannot fully explore the relationship between inhomogeneous microstructures of the left ventricle and diffusion metrics. To construct a realistic myocardium model, Rose et al. modeled myocytes with realistic cell morphologies extracted from histological images. With such a model, they simulated DTI with several imaging sequences, including pulsed gradient spin echo (PGSE), second-order motion compensated spin echo (M2−SE), and monopolar simulated echo acquisition mode (STEAM). They analyzed the effects of extra-cellular volume and diffusion coefficients (in both intra-cellular and extra-cellular spaces) on FA and mean diffusivity MD. However, without the corresponding real dMRI acquisitions, it is impossible to know whether the simulation results are consistent with real acquisitions.

The purpose of this work was to connect myocardial microscopic structures and macroscopic diffusion metrics based on a realistic cardiac DTI simulation. First, cardiac fiber orientations of the same human neonatal and infant hearts were obtained using both PLI and DTI. Since fiber orientations measured by PLI have been proven to be consistent with the Streeter's conjecture (D. Streeter,, 1979) and PLI is now considered a gold-standard technique for obtaining 3D fiber structure of *ex vivo* hearts with high spatial resolution (Jouk et al., 2007), we used physical measurements from PLI to model realistic cardiac fiber structures. Once the cardiac fiber model was constructed, DW images of such model were simulated by combining Bloch equation and Monte Carlo random walking. The simulations were then refined by adjusting the myocardium modeling parameters so that the simulated DTI metrics can match ~~with~~ the corresponding real acquired ones. ~~Following~~ that, we simulated DW images by varying myocyte arrangement pattern, extra-cellular volume, and myocyte size to investigate the relationship between tissue microstructure variations and macroscopic diffusion metrics.

2. METHODS

2.1. ~~Heart Preparation for~~ DTI and PLI

Five human neonatal and infant hearts were used for simulation. These hearts were obtained and processed in compliance with French legal and ethical guidelines. The investigations conformed to the principles outlined in the declaration of Helsinki (Carlson et al., 2004). First, all the hearts were embedded in a hydrophilic gel to maintain the shape of the heart. Then, the DW images of these *ex vivo* hearts were acquired with a 3T Siemens MRI scanner (MAGNETOM Verio) using a Siemens MDDW (multi-directional diffusion weighting) sequence. The characteristics and the corresponding acquisition parameters of each heart are given in Table 1. To increase the signal−to−noise ratio (SNR), all the DW images were acquired six times. Based on these DW images, diffusion tensor was calculated using the method proposed by Kingsley (Kingsley, 2006), from which cardiac fiber orientation and diffusion metrics including FA and MD were derived.

After DW image acquisition was accomplished, PLI of the same hearts was performed. PLI physically measures cardiac fiber orientations at a microscopic scale by detecting the birefringence of myosin filaments. To obtain cardiac fiber orientations with PLI, the heart was first perfused and fixed in a 4% neutralized formaldehyde solution and immersed for a minimum of one week in the same solution. Once fixed, the ventricular mass was then embedded in a hydrophobic acrylic resin, methyl methacrylate (MMA) prepared according to a well-defined protocol (Yang et al., 2018). Subsequently, the myocardium was dehydrated and impregnated first with a hydrophilic resin, methacrylate glyscol (GMA), and then impregnated with a mixture of GMA and MMA, in which the concentration of MMA was increased gradually until only MMA remained. The duration of the impregnations by successive baths was about 9 weeks. The whole heart sample was finally embedded by polymerization and reinforced by MMA resin. After the

Table 1. The characteristics and the corresponding DTI acquisition parameters of neonatal and infant hearts.

	Heart 1	Heart 2	Heart 3	Heart 4	Heart 5
Age	3 months	14 months	2 months	0 days	8 days
Weight	13.56 g	31.84 g	22.28 g	12.92 g	14.46 g
Septum thickness	6.3 mm	4.9 mm	4.4 mm	4.5 mm	3.7 mm
TE	70 ms	74 ms	70 ms	70 ms	70 ms
TR	5600 ms	5100 ms	5900 ms	7900 ms	5600 ms
Matrix size	104×104	104×104	104×104	104×104	104×104
Spatial resolution	1.38×1.38 mm^2	1.38×1.38 mm^2	1.38×1.38 mm^2	1.38×1.38 mm^2	1.38×1.38 mm^2
Slice thickness	1.4 mm	1.4 mm	1.4 mm	1.4 mm	1.4 mm
b value	700 s/mm^2	700 s/mm^2	700 s/mm^2	700 s/mm^2	700 s/mm^2
Number of diffusion directions	192	64	192	192	192

polymerization, the block of the sample was oriented and sectioned according to a selected reference frame with a slice thickness of 500 μm. 34 to 45 sections were collected with a spacing of 500 μm in a serial manner for the whole heart. For each section, images were acquired and fiber orientations were determined using the methods presented in the works of Jouk (Jouk et al., 2007) and Desrosiers (Desrosiers et al., 2016). The acquired raw PLI images are under the form of a series of paired two-dimensional (2D) images, which form a 3D volume. Each pair of images represents an elevation angle image and an azimuth image (Fig.1), and gives the orientation of fiber in space. In the present work, the spatial resolution of PLI images was 0.093 ×0.093×0.5 mm^3. We used the fiber orientations provided by PLI for modeling and considered them as the ground truths, and refined the ~~simulation~~ by matching the simulated diffusion metrics with the corresponding real acquisition ones.

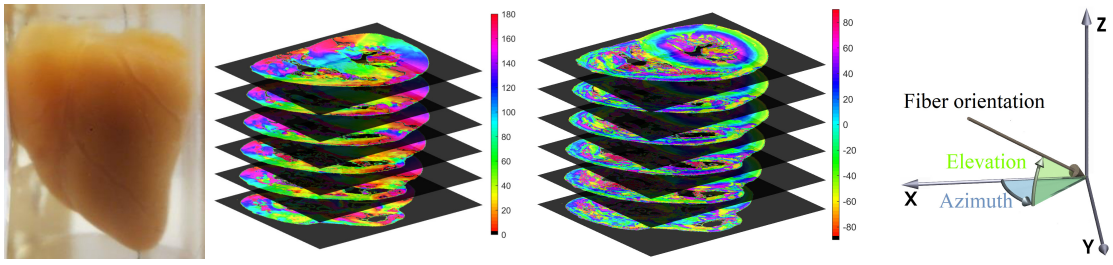

(a) (b) (c) (d)

Fig. 1. Fiber orientations of a neonatal heart obtained using PLI. (a) A neonatal heart specimen. (b) Azimuth angle maps for several neonatal heart sections. (c) Corresponding elevation angle maps, (d) Definition of elevation and azimuth angles.

2.2. Microstructure Modeling

The myocardium is mainly composed of myocytes connected end−to−end by intercalated discs and surrounded by an extracellular matrix. The myocytes are assumed to be quasi−parallel cylinders. Based on such anatomical characteristics and the fiber orientation maps measured by PLI, we modeled, in each voxel of PLI, a local myocardium using quasi-parallel packed cylinders. The geometrical modeling of such cylinder bundles can be reduced to a 2D circle packing problem. Namely, packing the cylinders is equivalent to packing the non−compressible and non−overlapped disks. Previous histological research showed that the distribution of myocyte diameters follows a natural logarithmic function. Therefore, in the modeling, the diameters of disks, which represent those of myocytes, were chosen randomly with a Hasting Metropolis algorithm using a log normal distribution with a mean μ_d and a standard deviation σ_d. The initial positions of these disks were randomly distributed within a square area of size $\sqrt{N \times \max(d_k, k = 1, 2, ..., N) + \Delta_d)^2}$, where N is the number of disks, d_k represents the diameter of the k^{th} disk, and Δ_d indicates the

maximum gap between different disks. Changing such gap varies the extra-cellular volume (ECV). The width of this square was determined by $\sqrt{N}+1$. In addition, in our modeling, myocyte membrane thickness was also considered, which was determined by internal myocyte diameter to external diameter ratio d_{ratio}. These disks were then migrated toward the area center using a molecular dynamics−based method (Mingasson et al., 2017) until the desired disk density was achieved.

Once the circle packing was completed, according to the fiber orientation at the current PLI image voxel, the geometrical structure of local myocardium was constructed. Firstly, we divided a PLI voxel into 20 subregions with a size of 46.5×46.5×100 μm^3. In each subregion, we assume that all the myocytes have the same orientation, which is derived as follows: according to the elevation and azimuth angles provided by PLI, calculating the fiber orientation and then rotating this orientation around itself by an angle φ, which is uniformly chosen from the range between 0 and *hetero*. Then, according to the orientation in each subregion, the packed circles were rotated and extruded to form paralleled and orientated cylinders. These cylinders intersect with the boundaries of subregions. Finally, only the cylinders located inside the subregions were kept and cut randomly into several segments according to the length range $[l_{min}, l_{max}]$ of myocytes and the length l_{dics} of intercalated disc. The detailed modeling process is illustrated in Fig. 2. The values of the corresponding modeling parameters are listed in Table 2, where as the values are expressed by range, they are assumed to be uniformly distributed.

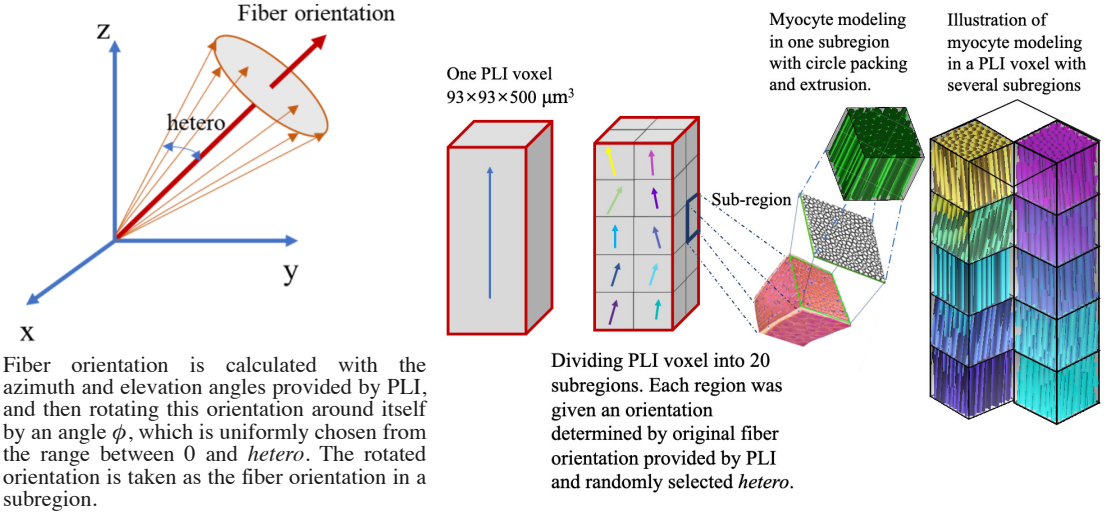

Fig. 2. Myocardium modeling process.

Table 2. Cardiac myocyte modeling parameters.

Parameter	Symbol	Value	Unit	References
Mean of diameter	μ_d	[6-10]	μm	(Wah and Keller, 2003)
STD of diameter	σ_d	1	μm	(Poole-Wilson, 1995; Pluess et al., 2014)
Length	l	[40-100]	μm	(Poole-Wilson, 1995)
Intercalated disc length	l_{disc}	3.3±0.4 (mean±std)	$10^{-2}\mu m$	(Hoyt et al., 1989)
Orientation heterogeneity	*hetero*	[0-30]	°	
Maximum gap between myocytes	Δ_d	[0-4]	μm	
Ratio of internal to external diameter	d_{ratio}	0.9		

2.3. *Diffusion MRI Simulation Framework*

We combined Bloch equation and Monte Carlo random walk simulation to produce realistic DW images. The Bloch equation was used to generate B_0 image and Monte Carlo random walk simulation was for providing the diffusion displacement distribution in the microstructures. To achieve this, the simulation framework takes a pulse sequence, a labeled object and a microscopic fiber structure as inputs, as depicted in Fig. 3(a). The details of the dMRI simulation are given in Fig. 3(c). The kernel of dMRI simulation includes geometrical modeling and Monte-Carlo random walking simulation. The former is described in Fig. 2 and the latter is illustrated in Fig. 3(b). The detailed simulation process is described as follows.

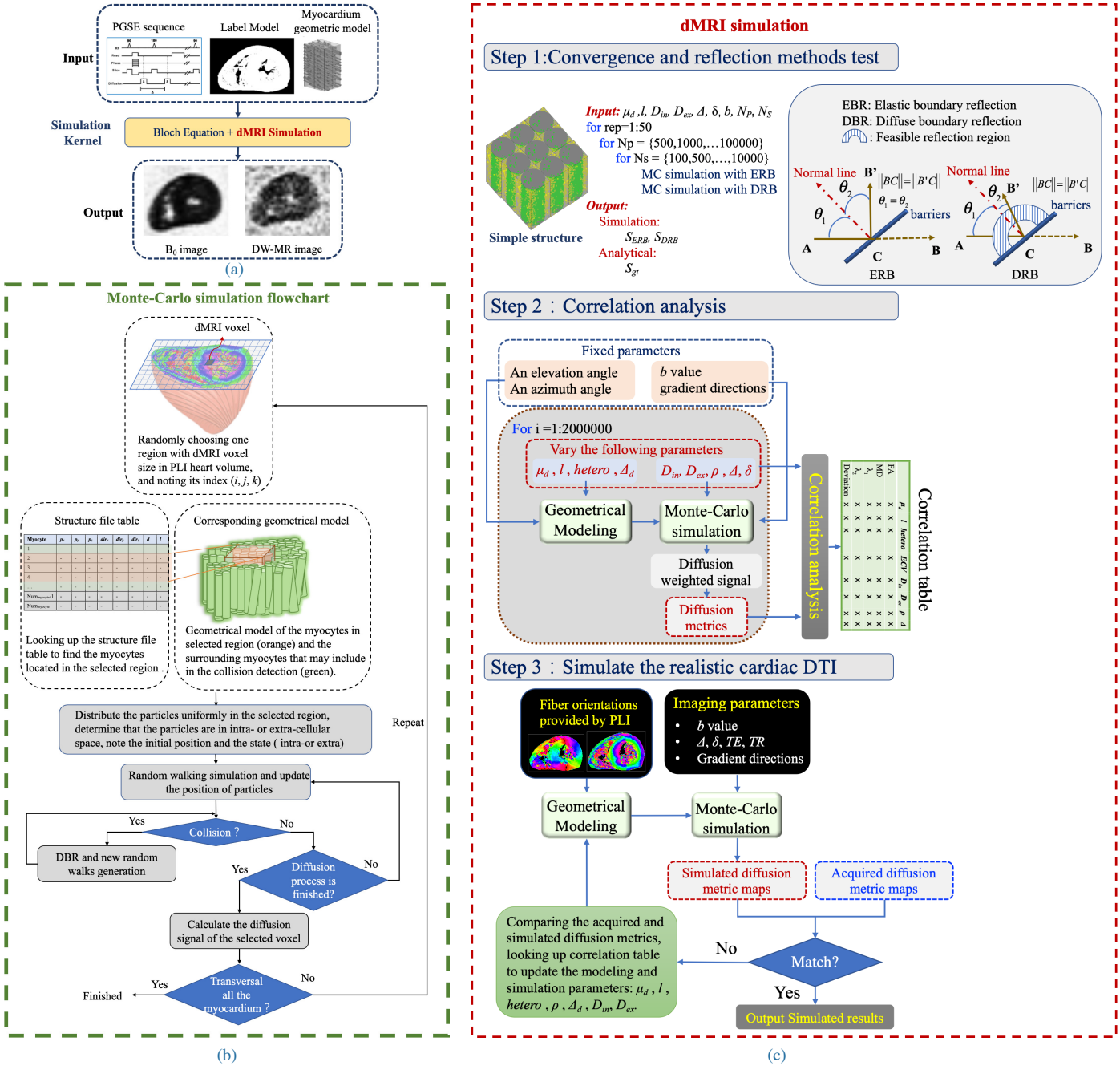

Fig. 3. Details of cardiac diffusion MRI simulation. (a) The overall simulation framework; (b) The flowchart of Monte-Carlo simulation in a cardiac model; (c) Detailed process of cardiac DTI simulation.

To simulate the B_0 image, the myocardium was segmented from PLI data. Then the proton density, T_1 and T_2 values of the

myocardium and background were given. For the cardiac muscle, T_1 was about 1471 *ms* and T_2 about 47 *ms* (Stanisz et al., 2005). For the background, T_1 and T_2 were chosen as 2000 *ms* and 70 *ms*, respectively. At each voxel of such a labeled object, the full MR (magnetic resonance) acquisition process was simulated by evolving magnetization vectors over time, which can be described as

$$\vec{M}_{t+1} = R_{relax} R_z R_{RF} \vec{M}_t, \tag{1}$$

where R_{RF} represents the rotation matrix caused by the RF pulse and given by

$$R_{RF} = \begin{bmatrix} 1 & 0 & 0 \\ 0 & \cos(\alpha) & \sin(\alpha) \\ 0 & -\sin(\alpha) & \cos(\alpha) \end{bmatrix}, \tag{2}$$

with α designating the flip angle. R_z describes the dephasing process induced by the imaging gradient and is expressed as

$$R_z = \begin{bmatrix} \cos(\theta) & \sin(\theta) & 0 \\ -\sin(\theta) & \cos(\theta) & 0 \\ 0 & 0 & 1 \end{bmatrix}, \tag{3}$$

where θ is the phase shift caused by the imaging gradients (phase and frequency encoding gradients), expressed by

$$\theta = \gamma \int_{t_0}^{t_0+\Delta t} \vec{r} \cdot \vec{G}(t) dt, \tag{4}$$

in which γ is gyromagnetic ratio, $\vec{r}$ the position in the label model, Δt the duration of imaging gradients, and $\vec{G}$ the gradient amplitude. R_{relax} indicates the relaxion process that can be described as

$$R_{relax} = diag\left(e^{-t/T_2}, e^{-t/T_2}, 1 - e^{-t/T_1}\right). \tag{5}$$

The transverse magnetizations M_x and M_y with various frequencies and phases are fulfilled in k-space and form a k-space data M,

$$M = \sum_{\vec{r}} M_x + j \sum_{\vec{r}} M_y. \tag{6}$$

Subsequently, Fourier transform is then applied on M to generate the spatial domain MR image S_0.

To obtain DW images of whole heart and to facilitate parallel simulation, we simulated diffusion weighted signals in a voxel-by-voxel manner, as illustrated in Fig. 3(b). The original PLI heart volume was split into regions of size equal to DTI voxel dimension. Then, one region was randomly selected. By looking up the structure file table, in which the locations, directions, diameters and lengths of all the myocytes are recorded, we searched for the myocytes located in the selected region (orange cylinders in Fig. 3(b)). Particles were distributed uniformly in the selected region and were determined in intra- or extra-cellular spaces. The initial position and state (intra- or extra-cellular space) of each particle was noted. The diffusion of water molecules in both intra- and extra-cellular spaces was described by a random walking process. In each walking step of duration τ, the diffusion displacements of intra- and extra-cellular molecules are described by

$$\begin{array}{l} r_{in} = \sqrt{6 D_{in} \tau} \\ r_{ex} = \sqrt{6 D_{ex} \tau} \end{array}. \tag{7}$$

where D_{in} and D_{ex} are the diffusion coefficients respectively in intra-cellular and extra-cellular spaces, which are smaller or equal to free diffusion coefficient $D_0 = 3 \times 10^{-3} mm^2/s$. To accelerate the diffusion simulation, the myocytes in the surrounding regions (extending the selected region by 2 times maximum diffusion displacement in one random walking step) that may be collided with the particles are selected (green cylinders in Fig. 3(b)). After each walking step, the collision between a segment and cylinders

(orange and green ones in Fig. 3(b)) was detected. If collision occurs, the particles will diffuse along the other directions without any energy loss. Conventionally, elastic boundary reflection (EBR) is usually used to deal with the collision between particles and membranes. However, this is time consuming. To deal with such issue, we proposed to use diffuse boundary reflection (DBR) to treat the collision (Xing et al., 2013; Fieremans and Lee, 2018). That is, when the particle collides with boundary, it is reflected by the membrane in a random direction to the next position located on the same side as its previous one. The difference between EBR and DBR is illustrated in Fig. 3(c) (Step 1). When the selected region is located at the boundary of the myocardium, the imaged object in a voxel may include partially the heart muscle and hydrophilic gel. In this case, part of free diffusion should be considered:

$$r_{free} = \sqrt{6D_0\tau} \tag{8}$$

The permeability of the membrane is about $0-100\ \mu m/s$ (Kuchel and Durrant, 1999; Fieremans et al., 2011). For a short diffusion time, although some molecules can pass through the membrane, their effect is negligible. Therefore, water exchange between intra− and extra−cellular spaces was not considered in the present work. During diffusion time Δ, phase shift caused by diffusion of one molecule i can be expressed as

$$\phi_i = \sum_{j=0}^{K} \vec{q} \cdot \vec{r}_i^{\,j}, \tag{9}$$

where $\vec{q}$ is the wave vector determined by diffusion gradient strength and duration, $\vec{r}_i^{\,j}$ indicates the position of the i^{th} particle after the j^{th} walking steps, and K is the total number of steps, $K = (\Delta - \delta/3)/\tau$. ϕ_i can be introduced by intra-cellular, extra-cellular space diffusion and free diffusion, noted as ϕ_{iintra}, ϕ_{iextra} and ϕ_{ifree}, respectively. The diffusion signal attenuation caused by all the molecules can be written as,

$$\frac{s}{s_0} = \frac{1}{N_{intra}+N_{extra}+N_{free}} \sqrt{\begin{array}{l}\left(\sum_{i=1}^{N_{intra}} \cos\left(\phi_{iintra}\right) + \sum_{i=1}^{N_{extra}} \cos\left(\phi_{iextra}\right) + \sum_{i=1}^{N_{free}} \cos\left(\phi_{ifree}\right)\right)^2 \\ + \left(\sum_{i=1}^{N_{intra}} \sin\left(\phi_{iintra}\right) + \sum_{i=1}^{N_{extra}} \sin\left(\phi_{iextra}\right) + \sum_{i=1}^{N_{free}} \sin\left(\phi_{ifree}\right)\right)^2\end{array}}, \tag{10}$$

where s is the diffusion weighted signal, s_0 is the signal without diffusion weighting (i.e. B_0 signal), N_{intra}, N_{extra} and N_{free} designate the effective number of water molecules for intra-cellular, extra-cellular and free diffusions, respectively. N_{free} is determined by the portion of free diffusion, namely the portion of hydrophilic gel. If the imaged region does not contain hydrophilic gel, $N_{free} = 0$. Considering that there may be immobilized water molecules in intra-cellular space (Aliev et al., 2002), we assumed that the diffusible water molecule density in intra-cellular and extra-cellular spaces may be different. Thus, the ratio of particle number in intra-cellular space to that in extra-cellular space may not be equal to the ratio of intra-cellular volume to extra-cellular volume. ~~Assuming~~ that the ratio of diffusible water molecules density in intra-cellular space to that in extra-cellular space is denoted as ρ. When calculating diffusion weighted signals, the effective number of particles in intra-cellular space (N_{intra}) and that in extra-cellular space (N_{extra}) are calibrated with: $N_{intra} = N'_{intra} \times \rho, N_{extra} = N'_{extra}$, in which N'_{intra} and N'_{extra} designate the original number of water molecules for intra-cellular and extra-cellular spaces, respectively.

Rician noise was finally added to the diffusion signals to simulate a realistic acquired image, described by

$$S_{noisy} = \sqrt{(s+\eta_1)^2 + \eta_2^2}, \tag{11}$$

where η_1 and η_2 conform to a normal distribution, namely $\eta_1, \eta_2 \sim \mathcal{N}\left(0, \sigma^2\right)$, with the standard deviation $\sigma = 1/\mathrm{SNR}$ controlling the level of noise. Note that the SNR here indicates the SNR of B_0 image.

The accuracy of Monte-Carlo random walking simulation depends on the number of particles, random walking steps and boundary collision method. To choose appropriate number of particles and steps and to validate the effectiveness of the collision method used in this work, we first performed the convergence test like that done in the work of Hall et al. (Hall and Alexander, 2009). ~~In~~ consists of using two boundary collision methods to quantify the variations of diffusion signals with the number of particles and steps in a fixed substrate, as illustrated in Fig. 3(c) (Step 1). Such substrate includes 200 parallel-packed cylinders with a mean diameter of 8 μm and a standard deviation of 1 μm; the length of cylinders is 1000 μm. The gap between cylinders is 1 μm. The diffusion coefficients in intra-cellular and extra-cellular spaces were assigned to 2×10^{-3} mm^2/s and 3×10^{-3} mm^2/s, respectively. Then, DW signals were simulated with different number of particles (500, 1000, 5000, 10000, 20000, 50000, 100000) and different number of steps (100, 500, 1000, 3000, 5000, 10000). Other simulation parameters are diffusion time $\Delta = 26\,ms$, gradient duration $\delta = 2\,ms$, and b value = 700 s/mm^2. For each combination of particle number and step, simulation was repeated 50 times with different random seeds. The convergence was evaluated in terms of relative mean absolute error (RMAE) of DW signals with respect to the analytical solution. The analytical signal generated by intra-cellular space of a cylinder of radius R is approximated by (Vangelderen et al.)

$$\frac{s}{s_0} = \exp\left(-2\gamma^2 g^2 \sum_{m=1}^{\infty} \frac{2D_{in}\alpha_m^2\delta - 2 + 2e^{-D_{in}\alpha_m^2\delta} + 2e^{-D_{in}\alpha_m^2} - e^{-D_{in}\alpha_m^2(\Delta-\delta)} - e^{-D_{in}\alpha_m^2(\Delta+\delta)}}{D_{in}^2\alpha_m^6\,(R^2\alpha_m^2 - 1)}\right) \tag{12}$$

where γ is the gyromagnetic ratio, g is the diffusion gradient strength, and a_m ~~are~~ obtained by dividing the roots of the first derivate of the Bessel function of the first kind by R. The analytical signal (i.e. ground truth) generated by multiple cylinders can be expressed as:

$$s_{gt} = \frac{\sum_{j=1}^{n} v_j s_j}{\sum_{j=1}^{n} v_j} \tag{13}$$

where s_j denotes the signal generated by j^{th} cylinder (calculated with Eq. (12)), v_j the volume of j^{th} cylinder and n the number of cylinders involved in the substrate. The RMAE between the simulated and analytical signals is defined by:

$$\text{RMAE} = \sum_{i=1}^{reps} \frac{s_{simu}^i - s_{gt}}{s_{gt}} \tag{14}$$

where $reps$ designates the number of repetitions equal to 50 and s_{simu}^i the signal obtained from i^{th} simulation.

Once the number of particles and steps were determined and the boundary collision method was validated, we analyzed the the correlations between modeling and simulation parameters and diffusion metrics to find the most possible substrate structure allowing us to generate realistic cardiac DTI simulation. As illustrated in Fig. 3(c) (Step 2), ~~A~~after fixing fiber orientation, b value and diffusion gradient direction, ~~by varying modeling and simulation parameters,~~ we obtain various substrates and simulation schemes. For example, in the present study, mean myocyte diameter μ_d of neonatal hearts in a voxel was varied from 6 to 10 μm, standard deviation of diameters was set as 1 μm , mean length $meanL$ of myocytes was changed from 40 to 100 μm, gap Δ_d between two myocytes was set between 0 and 4 μm , intra- and extra-cellular diffusion coefficients were varied from 0.5 to 3×10^{-3} mm^2/s, and ratio ρ of diffusible water molecule density in intra-cellular space to that in extra-cellular space was increased from 0.5 to 1. Diffusion time was changed from 20 ms to 50 ms, and diffusion gradient duration from 5 ms to 20 ms. With random combinations of the above parameter values, we generated 200 thousand combinations of substrates and acquisition schemes, and simulated the corresponding DW signals. After that, correlations between modeling/simulation parameters and diffusion metrics were analyzed, through which we identified what kind of parameters influence positively or negatively a given diffusion metric.

~~In the case of~~ real DTI acquisitions, we ~~used~~ an iterative method to find appropriate modeling and simulation parameters ~~to simulate realistic cardiac DTI (Fig. 3(c) (Step 3).~~ After fixing acquisition schemes, modeling parameters (μ_d, *hetero*, and Δ_d) and simulation parameters (D_{in}, D_{ex} and ρ) were initialized according to heart properties, such as the priors about maturation development of the heart. Then, the virtual myocardium structure was constructed using these modeling parameters, the corresponding DW images were simulated and diffusion metric maps were calculated using the package DIPY (https://dipy.org). Finally, the simulated diffusion metrics or DW images were compared with acquisitions. If simulations and acquisitions are not matched, we update the modeling and simulation parameters based on the correlation table. For example, if the simulated FA value is larger than the acquired FA value but the MD value is smaller, we will change the modeling or simulation parameters that can decrease FA and increase MD simultaneously. The iterations were terminated until simulations match acquisitions. The matching degree was evaluated in terms of fiber orientation (defined by helix angle) and diffusion metrics such as FA, MD, λ_1, and λ_2. Since simulation was based on PLI measurements while the position of the hearts in PLI was not the same as that in DTI, the comparison was carried out in terms of distribution instead of in a voxel-by-voxel manner. A Kruskal-Wallis test, which is a non-parametric ANOVA version that can test if two groups with different sample sizes are significantly different or not, was performed to determine the significant difference (P<0.05) in diffusion metrics between simulations and acquisitions.

2.4. Effects of Microstructure Variation on cardiac DTI Metrics

The correlation analysis ~~described~~ above was ~~only~~ performed in a single voxel, which does not reflect the variation of macroscopic myocardium structure (such as the helix angle), with respect to myocardium microstructure. To further explore the relationship between macroscopic cardiac DTI measurements and myocardium microstructure, we selected an AHA zone (AHA 12, mid anterolateral) from heart 1, where a number of myocardium models were constructed by changing ECV, myocyte diameter, and orientation heterogeneity of myocytes. Finally, we constructed five myocardium models with different ECV ratios (15%, 25%, 35%, 45% and 55%), five myocardium models with different orientation heterogeneities (0°, 5°, 10°, 15°, and 20°), and five myocardium models with different myocyte diameters (6 μm, 7 μm, 8 μm, 9 μm and 10 μm). In total, the corresponding DW images of 15 myocardium models were simulated with D_{in} =1×10^{-3} mm^2/s, D_{ex} =3×10^{-3} mm^2/s, Δ = 26 ms, δ = 20 ms, and b-value =700 s/mm^2. Following that, relationships between microstructure and macroscopic DTI measurements were analyzed.

3. Experiments and Results

3.1. Simulated B_0 Images

Based on the label model and the corresponding T_1 and T_2 values, the B_0 image was simulated with the following parameters: TE=70 ms, TR=7700 ms, static field strength=3T, FOV=104 × 104, and in-plane image resolution= 1.38 × 1.38 mm^2. Fig. 4 compares the simulated and acquired B_0 images, which have no significant difference in normalized intensity distribution (p = 0.29), which validates our B_0 image simulation method.

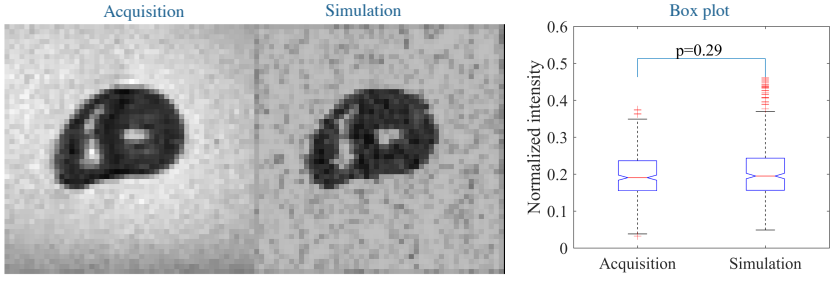

Fig. 4. Qualitative (visualization) and quantitative (box plot with p-value) comparisons between simulated and acquired B_0 images of the heart 1. The intensity of B0 image was normalized by dividing its own maximum value, and p-value was calculated with myocardium regions.

3.2. *Influence of Modeling and Simulation Parameters on DTI Metrics in a Single Voxel*

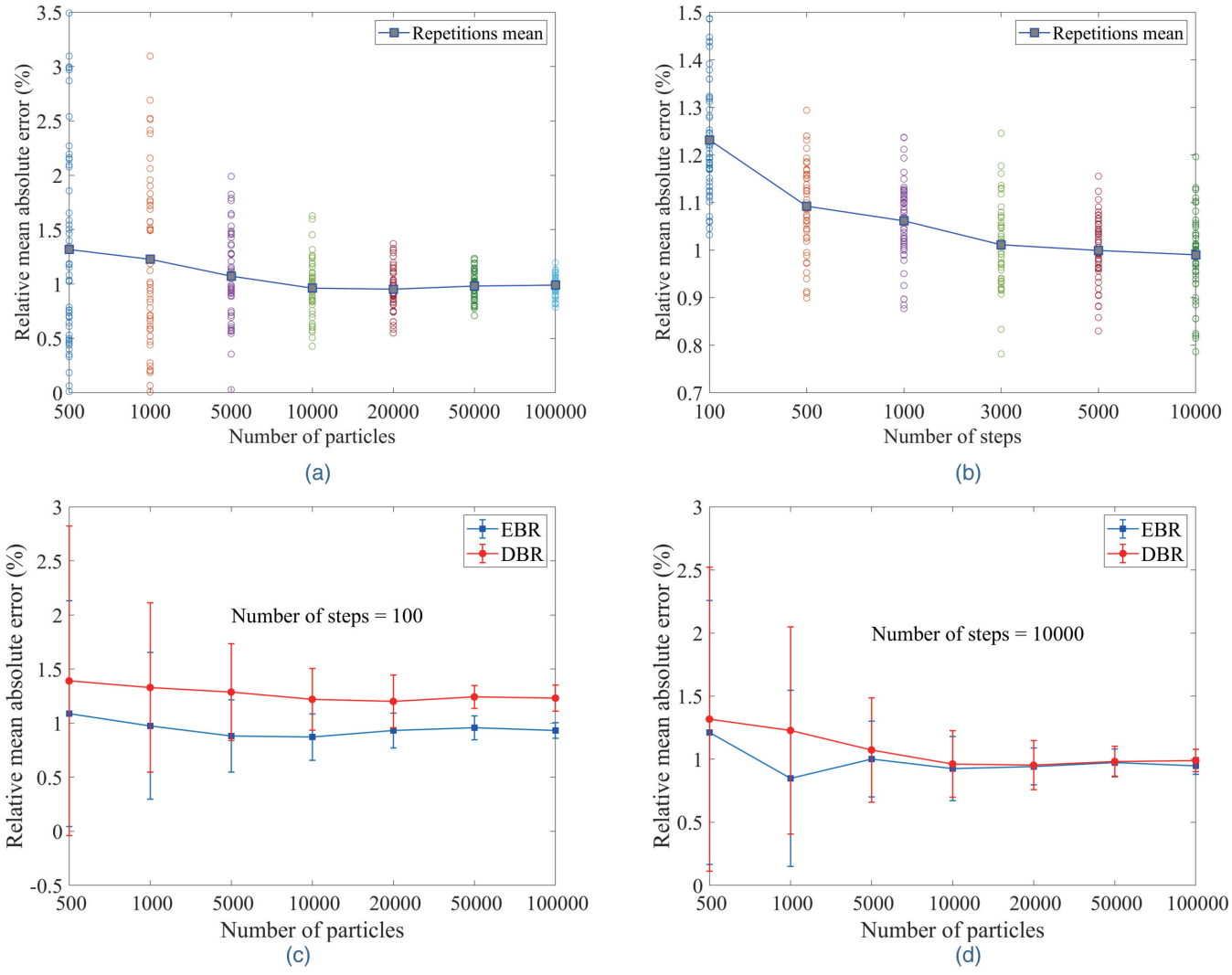

Fig. 5. Effects of the number of particles, walking steps and boundary reflection method on simulation signals. (a) Influence of number of particles for a given number of walking steps of 10000; (b) Influence of number of walking steps for a given number of particles of 100000; (c) Difference in RMAE of diffusion signals between elastic boundary reflection (EBR) and diffuse boundary reflection (DBR) obtained with different particle numbers and a fixed walking step number of 100; (d) Difference between EBR and DBR for a given number of walking step of 10000. The blue squares represent the RMAE of diffusion signals, and the circles indicate the relative absolute error (RAE) of diffusion signal for each repetition.

The variation of errors in diffusion signals as a function of particles or walking steps is shown in Fig. 5. As observed in Fig. 5(a), ~~as~~ the number of particles is larger than 10000, RMAE between simulation and analytical ground truth is always about 1%. Also, the more the number of particles there is, the smaller the standard deviation of RMAE becomes. Concerning the influence of number of walking steps (Fig. 5(b)), when the latter reaches 3000, RMAE tends to be stable with a value of about 1%, and the variation of RMAE caused by number of steps is not obvious. When varying number of steps from 100 to 10000, RMAE decreases about by 0.2%. Fig. 5(c) and (d) shows the difference between EBR and DBR in terms of simulated signal error; there is no obvious difference between them when the number of particles is larger than 5000 (for a given number of steps of 10000). However, when the number of steps is 100, the error of DBR is always larger than EBR, but not significantly (by about 0.4%).

According to the results of convergence test, the number of particles was set as 30000 and the number of walking steps as 5000 for the correlation analysis. The DW images of 200 thousand combinations of different substrates and acquisition schemes

described in section 2.3 were simulated. The influences of modeling and simulation parameters on diffusion metrics, including FA, MD, λ_1 and λ_2, and estimation accuracy of fiber orientations, were analyzed by means of the correlation heatmap, as illustrated in Fig. 6. We observe that FA is positively correlated with diffusion time (Δ), ratio of water molecule density in intra-cellular space to that in extra-cellular space (ρ), and diffusion coefficient in intra-cellular space (D_{in}). It is negatively correlated with mean diameter (μ_d), orientation heterogeneity (*hetero*) of myocytes and ECV. As to the first eigenvalue λ_1, it is positively correlated to diameter and length of myocyte, ECV, diffusion coefficients in both intracellular and extracellular spaces and diffusion time. It is negatively correlated to orientation heterogeneity and water molecule density ratio. The second eigenvalue λ_2 and MD are negatively correlated with water molecule density ratio and diffusion time. Concerning fiber orientations, the estimation error increases if mean diameter, orientation heterogeneity, ECV, and diffusion coefficient in extra-cellular space increase, and it decreases if diffusion time, diffusion coefficients in intra-cellular space and water molecules density ratio increase. Based on such correlations and comparison with real acquisitions, along with the constraints of priors about the maturation development of hearts, we can adjust our modeling and simulation parameters to realize realistic cardiac DTI simulation.

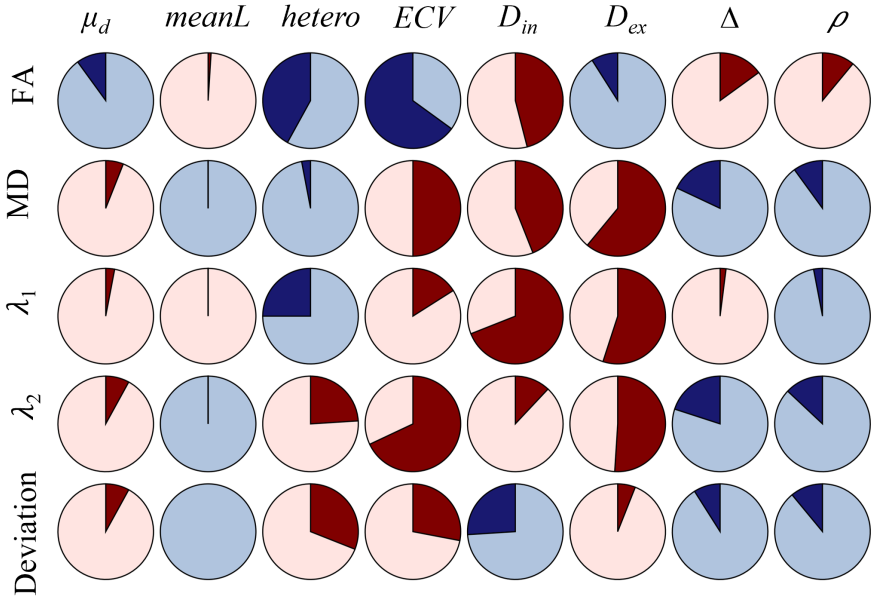

Fig. 6. Correlation between microscopic myocardial structure parameters and macroscopic DTI measurements. "μ_d" indicates the mean diameter of myocytes, "*meanL*" the mean length of myocytes, "*hetero*" the orientation heterogeneity, "*ECV*" the extra-cellular volume ratio. "D_{in}" and "D_{ex}" are the diffusion coefficients in intra- and extra-cellular spaces respectively. "Δ" is the diffusion time, and "ρ" the ratio of water molecule density in intra- to extra-cellular spaces. The red clockwise pie chart represents the positive correlation, the counterclockwise blue pie chart depicts the negative correlation, and the proportion of dark blue or dark red indicates the strength of correlation. The light red full circle represents the maximum positive correlation coefficient with a value equal to 1. The light blue full circle represents the maximum negative correlation coefficient with a value equal to -1.

3.3. Cardiac DTI Simulation Results

Based on real acquisitions and correlations between modeling / simulation parameters and diffusion metrics, the final modeling and simulation parameters for the five hearts are given as follows: the mean myocyte diameters for the heart 1, heart 2, heart 3, heart 4 and heart 5 are 9.5, 10, 9, 7, and 8 μm respectively; the standard deviation of the diameters in a PLI voxel is 1 μm; the maximum gap between myocytes for the five hearts are respectively 3 μm, 0.5 μm, 3.5 μm, 3 μm, and 3.5 μm; the mean length of myocytes is 80 μm; the orientation heterogeneities are 25 °, 20 °, 28 °, 25° and 30 °; the ratio of diffusible water molecular density in intra-cellular space to that in extra-cellular space is 0.9, 0.95, 0.95, 0.99, and 0.99 respectively for the five hearts. The extracellular diffusion coefficient is fixed as 3×10^{-3} mm^2/s, and the intracellular diffusion coefficients for the five hearts are 0.9×10^{-3}, 0.45×10^{-3}, 1×10^{-3},

1.8×10^{-3}, and 1.1×10^{-3} mm^2/s respectively. With a diffusion time of 26 ms (except heart 2 for which the diffusion time is 30 ms), diffusion gradient pulse duration of 20 ms, walking step duration of 0.1 ms, diffusion direction number of 193 (except heart 2 for which the number of diffusion directions is 64), and b-values of 5, 700 and 705 s/mm^2, the simulated DW images along one diffusion direction for different infant hearts are shown in Fig. 7, together with the corresponding acquired ones and the statistical analysis. We observe that globally the simulated and acquired DW images have no significant difference with $p > 0.05$, which demonstrates that our simulation is realistic.

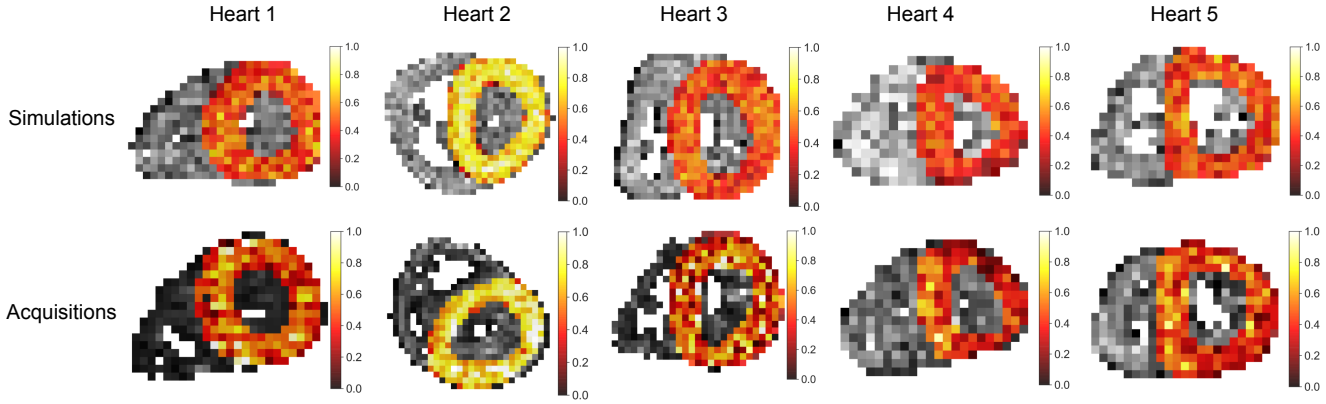

(a) DW images obtained from simulations and acquisitions for five hearts

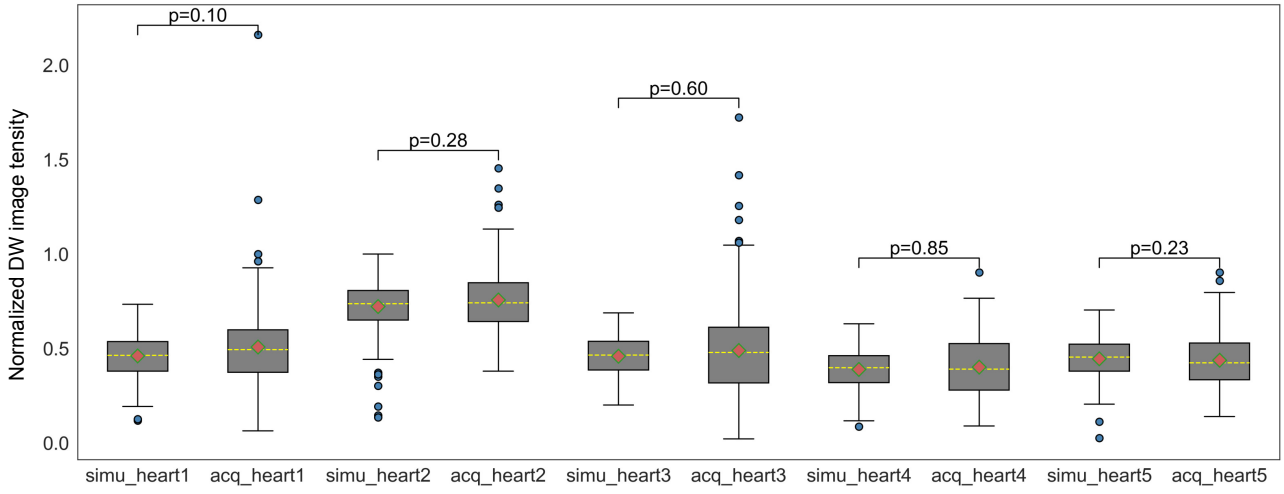

(b) Box plots of DW images along with p value

Fig. 7. Qualitative and quantitative comparison between simulated and acquired DW images along one diffusion direction for different hearts. Note that the intensity of DW images was normalized to [0, 1] by dividing B_0 image.

From the DW images, FA, MD, λ_1, λ_2 and fiber orientations were calculated. Note that, since helix angle is a well-known index for ~~describing~~ the cardiac fiber structure, we used it in the result section to describe fiber orientation. For PLI, helix angle was calculated from the orientation defined by elevation and azimuth angles. For simulated and acquired DTI, helix angle was calculated from the eigenvector with the largest eigenvalue. Comparisons of the simulated and acquired diffusion metrics for left ventricle are given in Fig. 8. Visually, we can see that the simulated and acquired FA, MD, λ_1, and λ_2 are very similar, except at the septum and free lateral, as illustrated in the red rectangle of Fig. 8.

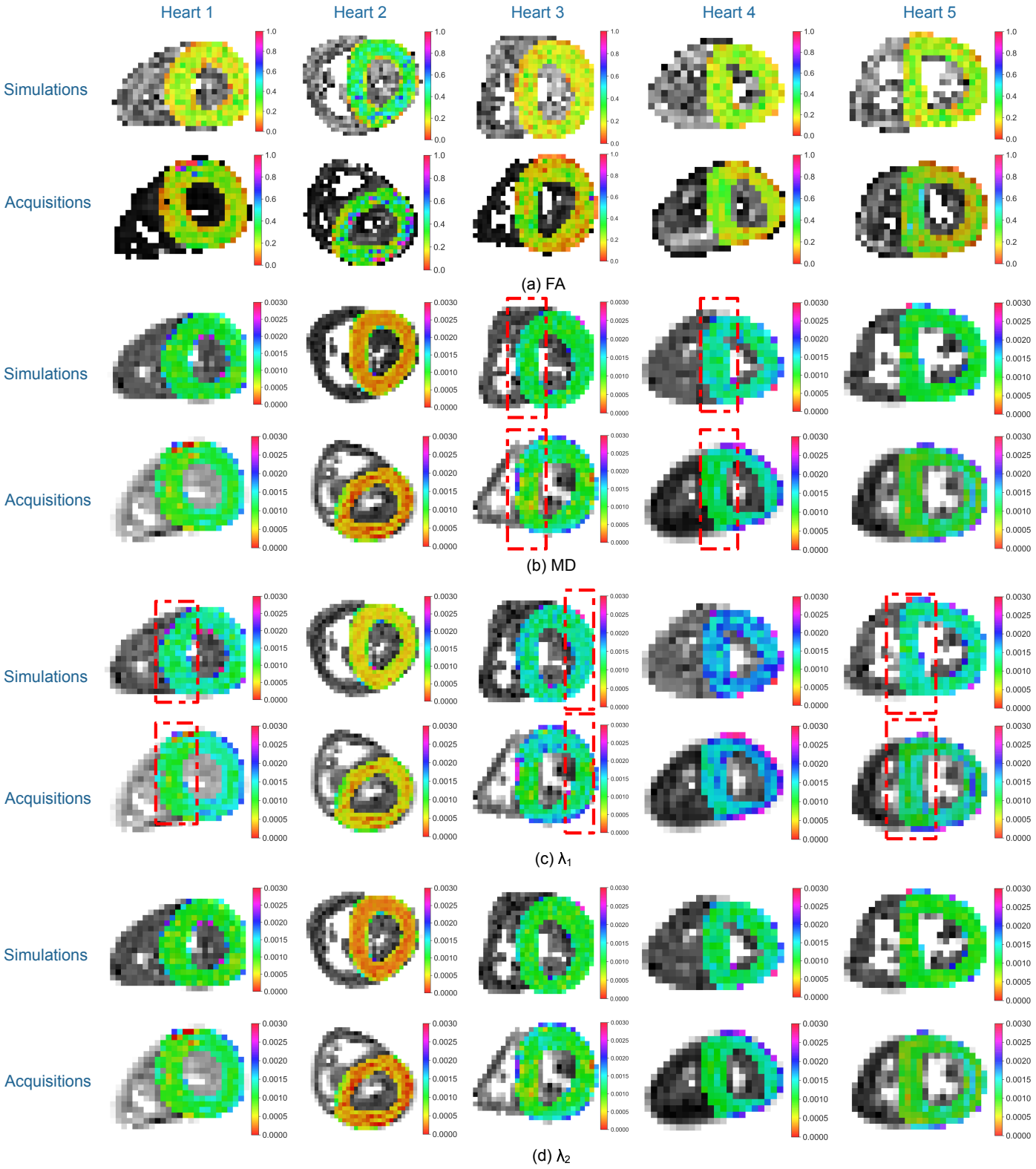

Fig. 8. Comparison between simulated and acquired diffusion metrics of five hearts, including FA, MD, λ_1, and λ_2. For fair comparison between simulations and acquisitions, as well as between different hearts, the range of FA is displayed between [0,1], and that of MD, λ_1 and λ_2 between [0, 0.003] (mm^2/s). The regions with major difference between simulations and acquisitions are highlighted with red rectangles.

To quantitatively compare the difference between simulations and real acquisitions, the box plots of FA, MD, λ_1 and λ_2 for both simulation and acquisitions of the five hearts are given in Fig. 9, in which, "simu" designates the simulation, and "acq" the

acquisition. For each group of diffusion metrics, p-value is annotated above the box plots. Notice that p-value for all the diffusion metrics is larger than 0.05, which means that there is no significant difference between the simulations and acquisitions.

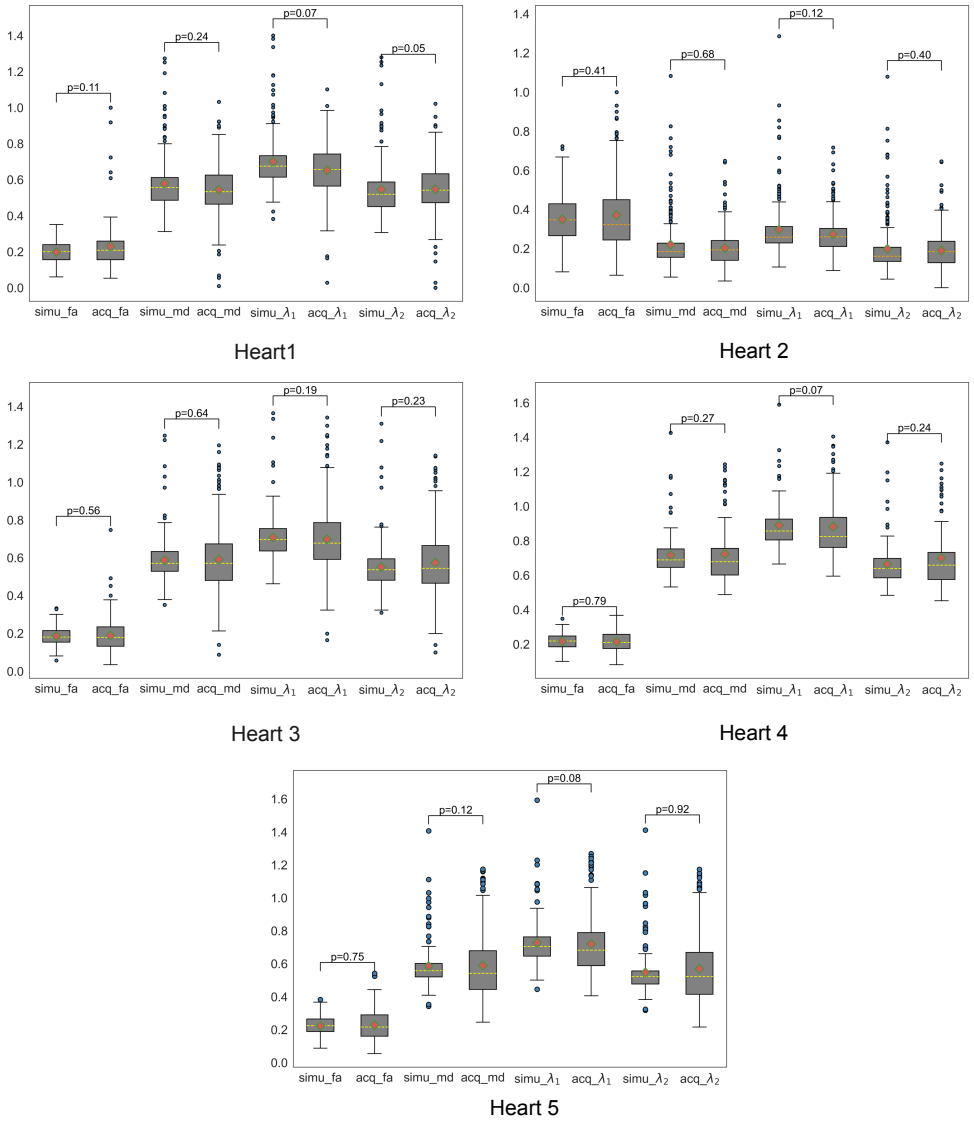

Fig. 9. Box plots of simulated and acquired diffusion metrics, including FA, MD, λ_1 and λ_2. Note that λ_1, λ_2 and MD were multiplied by 500.

In addition to the diffusion metrics, the helix angle maps of left ventricles extracted from PLI acquisitions, simulations and DTI acquisitions are shown in Fig .10. To evaluate our simulation with respect to PLI acquisitions, spatial resolution of PLI helix angle maps is scaled to DTI spatial resolution by averaging fiber orientations in multiple PLI voxels (Fig. 10 (b)). We observe that the simulated helix angle is almost the same as the scaled PLI helix angle except for a few pixels.

To quantitatively evaluate the difference in helix angle between simulations and real acquisitions, the box plots of helix angles and the corresponding p-values are provided in Fig .11. We see that, for all the hearts, the interquartile range of helix angles acquired by DTI is smaller than that acquired by PLI or simulations, which implies that helix angles from real DTI acquisitions are more concentrated. Moreover, there are significant differences in helix angle between DTI acquisitions and PLI acquisitions for heart 2 (with p = 0.01) and heart 3 (with p = 0.026). By comparing "PLI" and "PLI_with_DTI_VoxelSize", we found that the range of helix angles decreases when observing at a larger voxel. As to the helix angles obtained by simulations, they are similar not only to the initial helix angles from PLI but also to those from real DTI acquisitions (with p>0.05), except for heart 2 where the helix angle

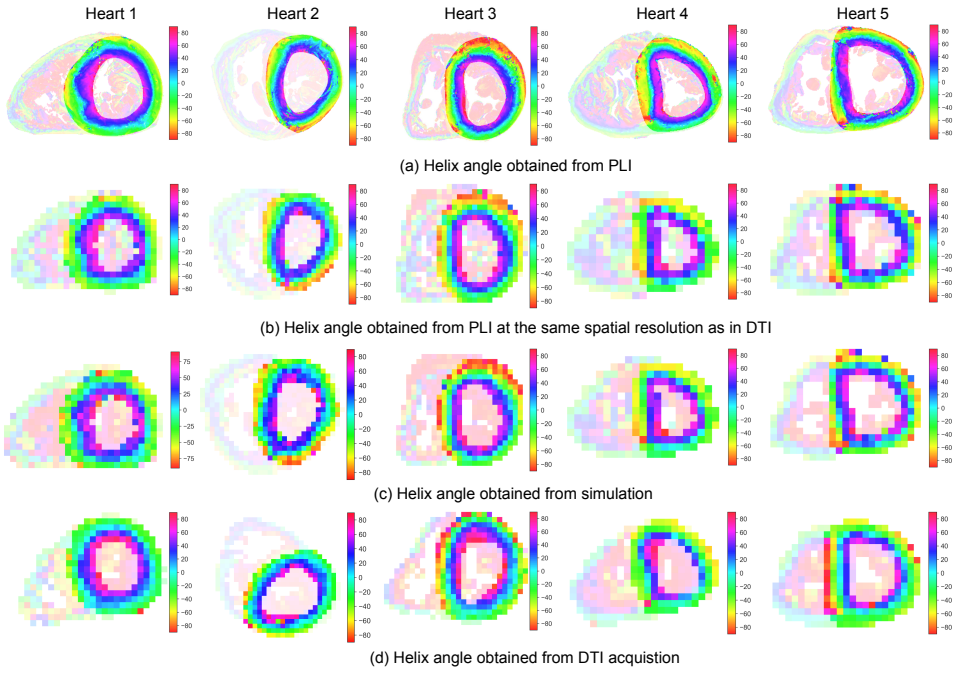

Fig. 10. Comparison between simulated and acquired DTI helix angles for 5 different hearts. The helix angle range is [-90,90].

from DTI acquisition is neither similar to the PLI acquisition nor to the simulation.

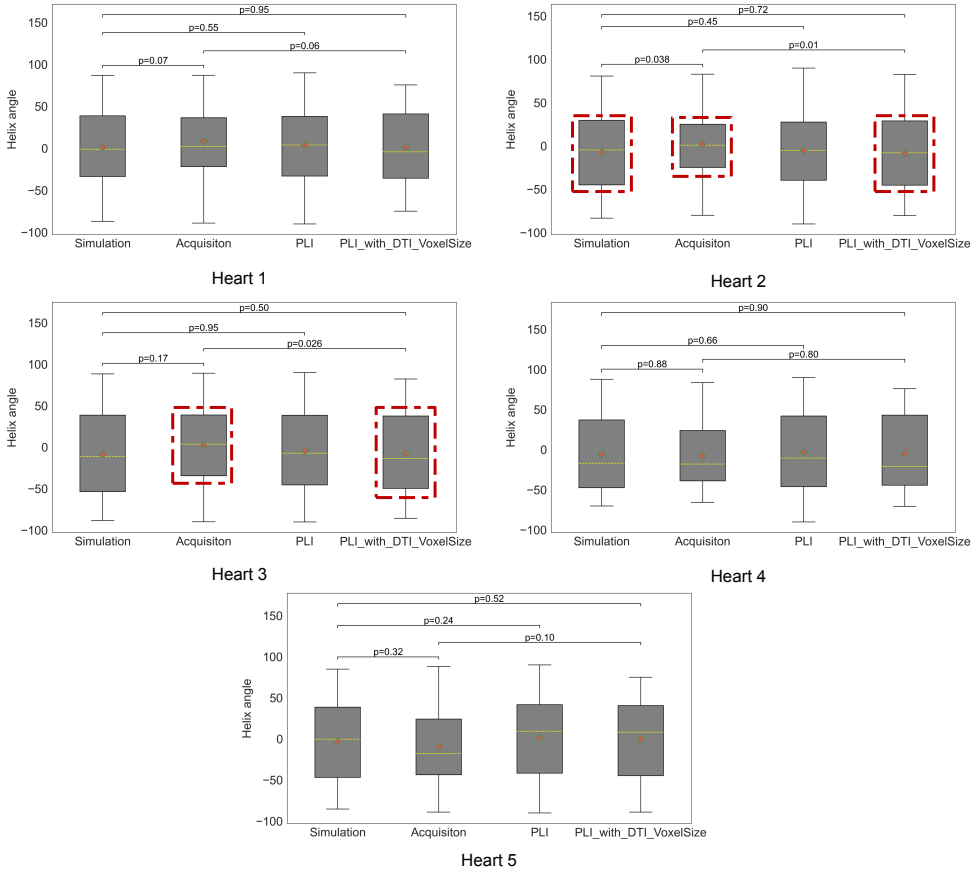

Fig. 11. Box plots of helix angles obtained by PLI, simulation and real DTI acquisitions. For the labels of x-axis, "simulation" is DTI simulation, "Acquisition" indicates DTI acquisition, "PLI" and "PLI_with_DTI_VoxelSize" represent the helix angle obtained by PLI at original resolution and DTI resolution respectively.

3.4. Variations in Myocardium Microscopic Structure against Macroscopic Cardiac Diffusion Metrics

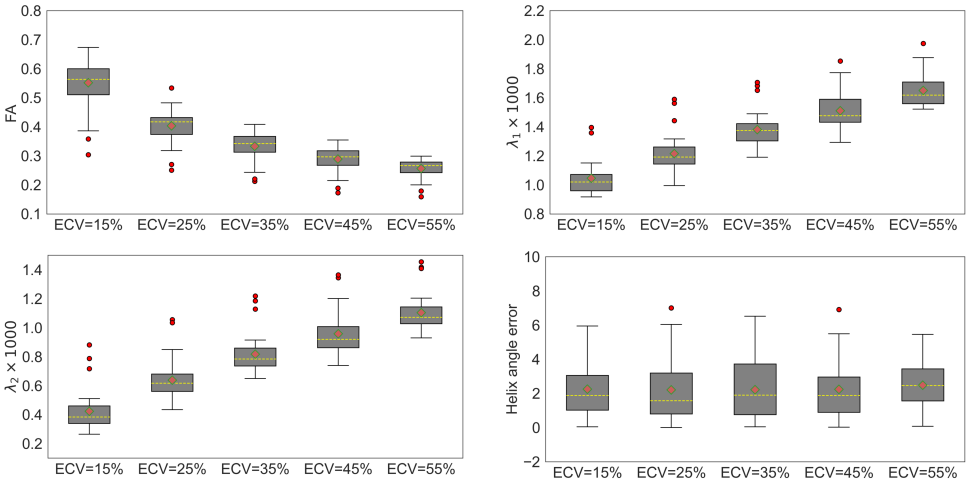

(a) Box plots of diffusion metrics as a function of ECV ratio

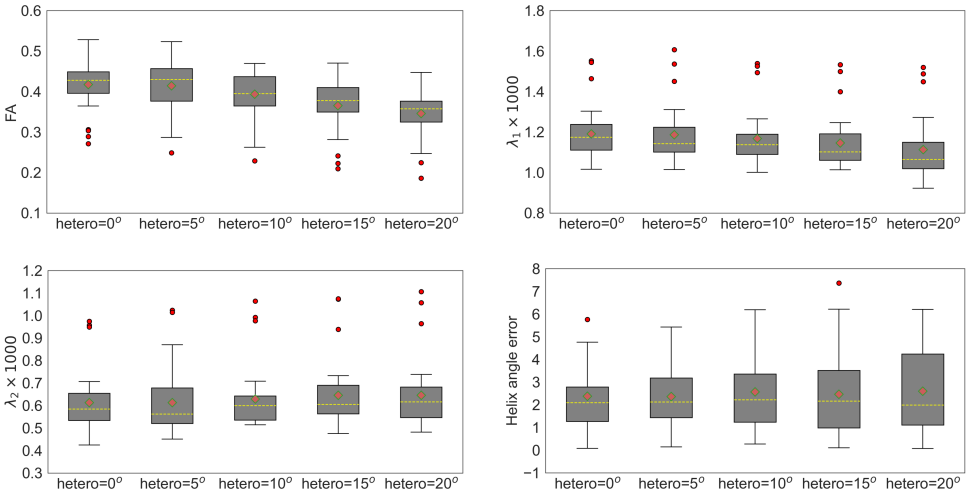

(b) Box plots of diffusion metrics as a function of orientation heterogeneity

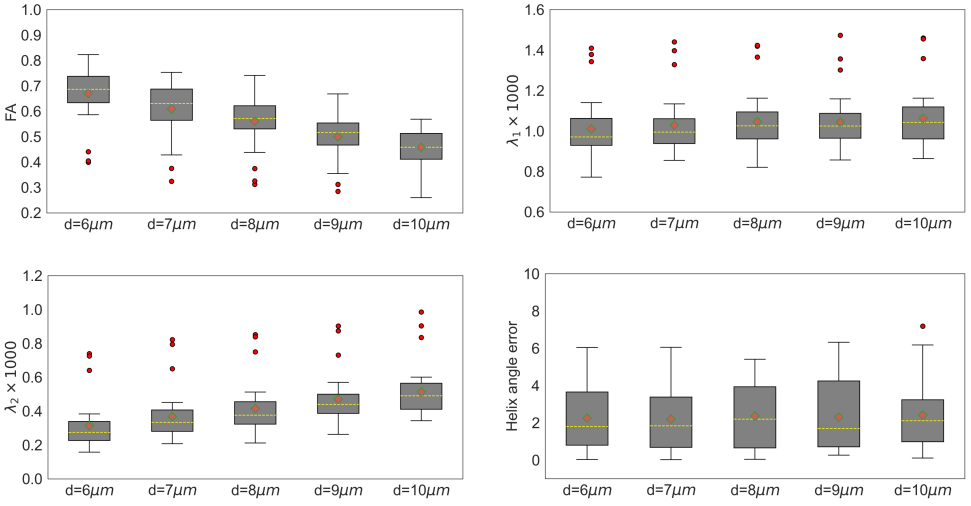

(c) Box plots of diffusion metrics as a function of myocyte diameter

Fig. 12. Effects of ECV ratio, orientation heterogeneity and myocyte size on diffusion metrics. In (a), mean diameter is 8 μm, orientation heterogeneity is 0 °, and myocyte length varies from 40-100 μm. In (b), mean diameter is 8 μm, maximum gap between myoctes is 1 μm, and myocyte length varies from 40-100 μm. In (c), orientation heterogeneity is 0 °, maximum gap between myoctes is 0 μm, and myocyte length varies from 40-100 μm.

With D_{in}=1 $\mu m^2/ms$ and D_{ex} = 3 $\mu m^2/ms$, we simulated the DW images of several myocardium structures in an AHA zone by varying the modeling parameters. Fig. 12 gives the effects of ECV ratio, orientation heterogeneity and myocyte size on diffusion metrics, including FA, λ_1, λ_2 and error in helix angles with respect to PLI ground-truth. The corresponding results are visualized in Appendix. From Fig. 12(a), we observe that with the increase of ECV, FA decreases and λ_1 increases but not significant with respect to λ_2. When varying ECV from 15% to 55%, mean FA decreased from 0.55 to 0.26, axial diffusivity increased by 0.6 $\mu m^2/ms$, and radial diffusivity increased by 0.7 $\mu m^2/ms$. Regarding helix angle, increasing ECV increases the mean error in helix angle. When orientation heterogeneity was varied from 0 ° to 20 °, mean FA decreased from 0.4 to 0.3 and axial diffusivity decreased by 0.08 $\mu m^2/ms$ but radial diffusivity increased by 0.03 $\mu m^2/ms$. The increase in radial diffusivity caused by orientation heterogeneity is not as obvious as the decrease in axial diffusivity. Concerning the estimation error of helix angle, when orientation heterogeneity increases, the interquartile range of helix angles errors increases, as illustrated in Fig. 12(b). The influences of myocyte size on diffusion metrics are illustrated in Fig. 12(c). Note that the increase of myocyte diameters resulted in a lower FA, a higher λ_1 and λ_2. When mean diameter of myocytes was varied from 6 μm to 10 μm, FA decreased from 0.67 to 0.46, λ_1 and λ_2 increased by respectively 0.05 and 0.2 $\mu m^2/ms$. Also, the mean values of helix angle errors increase when the myocyte diameter is increased.

4. Discussion

We have ~~investigated the relationship between macroscopic DTI diffusion metrics and myocardial microstructures~~ by ~~simulating~~ DW images of realistic myocardial model constructed based on high spatial-resolution PLI measurements. To get realistic simulation, we first performed DTI simulations in a single voxel with a large number of virtual structures that were modeled with the combination of all the possible modeling and simulation parameters. Then, by analyzing the correlations between diffusion metrics and modeling and simulation parameters, and by comparing with real acquisitions, we searched for appropriate modeling parameters to construct the right substrate for cardiac DTI simulation.

Considering the correlations between diffusion metrics and simulation parameters (including diffusion time Δ, diffusion coefficients D_{in} and D_{ex}, and ratio ρ of diffusible water molecules density in intra-cellular to extra-cellular space) in Fig. 6, we found that the variation trends of FA and diffusivities with Δ are consistent with the findings in the work of Kim et al. (Kim et al., 2005), in which when Δ varies from 33 ms to 412 ms, parallel diffusivity in calf hearts increases firstly (not significantly) and then remains almost unchanged, whereas perpendicular diffusivity decreases and FA increases. This phenomenon can also be found in *in vivo* cardiac DTI. For example, FA obtained with STEAM sequence is larger than that with M2-SE sequence, since diffusion time is much longer in STEAM compare to M2-SE sequence (Scott et al., 2018). As to the influence of D_{in}, we found that increasing D_{in} results in larger FA and MD, which is consistent with the findings reported by Rose et al. (Rose et al., 2019). Concerning the influence of D_{ex}, Rose et al. found that increasing D_{ex} did not affect FA but increased MD. However, our simulations demonstrated that the increase of D_{ex} led to a smaller FA and a larger MD. This can be explained by isotropic diffusion property in extra-cellular space. Increasing D_{ex} can increase simultaneously λ_1 and λ_2 by the same amount, denoted as $\Delta\lambda$. According to the definition of FA, $\mathrm{FA} = \sqrt{\frac{1}{2}}\frac{\sqrt{(\lambda_1-\lambda_2)^2+(\lambda_2-\lambda_3)^2+(\lambda_3-\lambda_1)^2}}{\sqrt{\lambda_1^2+\lambda_2^2+\lambda_3^2}}$, increasing λ_1, λ_2 and λ_3 by $\Delta\lambda$ at the same time does not change the numerator but increases the denominator of FA, thus resulting in the decrease of FA. In the work of Rose et al., such phenomenon was not observed. This may be caused by the fact that the variation ($\Delta\lambda$) of axial and radial diffusivities with D_{ex} was not obvious. As a result, FA was unaffected and MD increased non-significantly with the increase of D_{ex}. When comparing the influences of D_{in} and D_{ex} on FA, we found that the effect of D_{in} is more significant, which is in agreement with the findings of Rose et al. When the ratio of diffusible water molecule density in intra-cellular space to that in extra-cellular space increases, FA increases, but λ_1, λ_2 and MD decrease. The reason is that the restricted diffusion fraction increases, ~~therefore~~ leading to larger FA and smaller diffusivities.

To get a realistic cardiac DTI simulation, with the constraints of prior knowledge about the myocardium structure, the microstructure modeling parameters are iteratively refined by matching DTI simulations and real acquisitions of the same hearts. In practice, it is impossible to image the same hearts with DTI and PLI at exactly the same position and state. If we want to perform pixel-by-pixel comparison to determine ~~it is match or not~~, image registration would be required. However, registration may introduce unavoidable errors because myocardium is a deformable object. Therefore, we compared the simulations and acquisitions with similar slices that have almost the same ventricle volumes. The volumes measured by PLI for the five hearts in Fig. 7 are respectively 602, 925, 795, 385 and 433 mm^3, and the corresponding volumes measured by DTI are 625, 935, 769, 377 and 453 mm^3. This explains the slight difference in shape between DTI and PLI slices in Fig. 7. The statistical test showed that there is no significant difference between simulations and acquisitions in terms of DW images and diffusion metrics. However, from the visual results in Fig. 8, we found that there are still some differences between simulations and acquisitions at the free lateral and septum (red rectangle in Fig. 8). Such differences illustrate that the modeled structure in these zones may be different from the underlying ground-truth structure. In our method, the modeling parameters are homogeneous for the whole myocardium, which indicates that the mean diameter, orientation heterogeneity and ratio of diffusible water molecules density are set as the same everywhere. However, there are several studies on rat and pig hearts, which demonstrated that the myocyte diameters at the mid-myocardium, endocardium and epicardium are different (Gerdes et al., 1986; Campbell et al., 1987). In addition, with real DTI acquisitions of human hearts, it was found that both FA and MD are higher at septum than at lateral (McGill et al., 2015). However, our acquisitions for heart 3, heart 4 and heart 5 revealed that FA is greater at septum than at lateral, but that MD is smaller at septum than at lateral. On the other hand, the diffusion metrics of heart 2 were totally different from other hearts. Therefore, during the modeling, the mean myocyte diameter for this heart had been set as 10 μm, which is larger than the mean myocyte diameter of the other hearts. Likewise, the maximum gap between myocytes had been set as 0.5 μm and the orientation heterogeneity as 20 °, which is smaller than those of the other hearts. During the simulation, diffusion coefficient in intracellular space D_{in} was set as 0.5 $\mu m^2/ms$. Concerning the age of the hearts, we know that heart 2 is the oldest one. With the development of heart after birth, myocyte diameter, length and volumes increase, the gap between myocytes becomes narrower, and the content of sarcoplasmic reticulum and myofibrils inside the myocyte increases (Wah and Keller, 2003). We therefore assumed that the diffusion coefficients in intracellular space D_{in} decreases with the maturational development. According to correlation analysis results in Fig. 6, increasing diameter and decreasing D_{in} should decrease FA. However, with the decrease of ECV and orientation heterogeneity, FA increases. The combining effects of ECV and orientation heterogeneity are more significant than the effects of diameter and D_{in}. Accordingly, FA of heart 2 increases. Similarly, the decreasing effect of D_{in} and ECV on MD, $\lambda 1$, and λ_2 is more obvious, ~~therefore~~ resulting in smaller MD, $\lambda 1$, and λ_2 for heart 2. It has been demonstrated that with the aging of neonatal hearts, FA increases, both parallel and perpendicular diffusivities decrease (Pervolaraki et al., 2017). Our acquisition and simulation of heart 2 conform to these findings. With regard to the helix angles (Fig.10), the difference between simulations and acquisitions for all the hearts is not obvious. However, helix angles of heart 2 and heart 3 obtained by DTI and PLI acquisitions are different ($p < 0.05$ in Fig.11). This may be caused by DTI acquisition noise or slice difference between PLI and DTI. Although we have matched PLI slices and DTI slices with the closest volumes, it is still possible that these slices do not correspond exactly to the same myocardium positions, ~~thus~~ introducing the difference in helix angle.

By investigating the influences of the variations of ECV on diffusion metrics, we found that FA, λ_1, and λ_2 are correlated to ECV, which is consistent with recent reports (Ariga et al., 2019; Wu et al., 2018). As illustrated in Fig. 12(a), as ECV is increased, FA decreases, and λ_1 and λ_2 increase. Increasing ECV can reduce the hinderance effect for extra-cellular water molecules diffusion; ~~therefore,~~ axial and radial diffusivities in extra-cellular space increase, thus leading to the increase of λ_1, λ_2 and MD. Meanwhile,

with the increase of ECV, the fraction of isotropic diffusion increases, and that of anisotropic diffusion decreases; consequently, FA decreases.

Concerning the variation of diffusion metrics with respect to orientation heterogeneity (Fig. 12(b)), it can be explained as follows. An increase in orientation heterogeneity tends to destroy diffusion direction preference, which makes the diffusivity almost the same in all directions and thus decreases both FA and λ_1 and increases λ_2. As to the helix angle, the increase of heterogeneity will increase the uncertainty of estimated cardiac fiber orientations and consequently the large variation of helix angles, which can be clearly demonstrated by the variation of the estimation errors of helix angles.

The variation with myocyte diameter of FA, λ_2 and helix angle can be readily understood in light of the restricted diffusion in intracellular space. Larger myocyte diameter makes the intracellular diffusion less restricted along the myocyte radial direction, thus resulting in the increase of radial diffusivity λ_2 and the decrease of FA. Meanwhile, increasing the myocyte diameter decreases the difference in diffusion displacement between parallel and perpendicular directions. Accordingly, the directional preference of particle diffusion is decreased, leading to a large variation of estimation errors in helix angle. All these results are consistent with observations in studies on myocardium infarction. It is well known that myocardial infarction leads to the increase in myocyte cross-sectional area (diameter) (Gerdes et al., 1992), and that, in the infarct zones, FA decreases, MD increases, and helix angle experiences a larger variation (Nguyen et al., 2018a; Mekkaoui et al., 2018). As to the variation of axial diffusivity λ_1 with the myocyte diameter, in theory, it should not change with the diameter, however, in our work, we observe that increasing the diameter leads to an increase of λ_1 but not significantly. This is caused by collision treatment method DBR used in this work. With the traditional elastic boundary reflection (EBR) method, changing the diameter influences only the radial diffusivity and not the axial diffusivity. However, due to different reflection methods of dealing with collision, there is discrepancy in extracellular diffusion signals between EBR and DBR methods. More precisely, in EBR collision method, after collision, the particles can diffuse only along the reflected direction, while in DBR collision method, the particles can diffuse along any directions in the reflected plane. As a result, in a very small extracellular space, after collision, the particles diffusing with DBR method have larger probability to avoid colliding again with boundary. Accordingly, the extracellular particles can diffuse a longer distance along the perpendicular direction in DBR method, which makes that extracellular diffusion signals along perpendicular direction are more attenuated with DBR method than with EBR. Since the diffusion step size always keeps unchanged, bigger displacement along perpendicular direction leads to smaller displacement along parallel direction. Consequently, along parallel direction, the signal is less attenuated with DBR than with EBR. When increasing the myocyte diameter, the size of each extracellular diffusion pool increases and the collision difference between EBR and DBR is decreased. Accordingly, the discrepancy between EBR and DBR can be overlooked. By comparing EBR and DBR method, we observe that when the diameter is small, there is discrepancy in extracellular diffusion signals, but as the diameter is large enough, the discrepancy between EBR and DBR can be neglected. The change of discrepancy between EBR and DBR with the diameter leads to the change of axial diffusivity with diameter in our work, but such change is not significant and can be accepted.

With respect to cardiac DTI simulation of Rose et al. (Rose et al., 2019), which aimed to analyze the effects of D_{in}, D_{ex}, ECV and gradient strength on diffusion metrics with three different imaging sequences, although their model structures are realistic, the corresponding simulations were not sure to be realistic because real dMRI acquisitions were not used. Their simulated FA was higher than that reported in cardiac DTI literatures. In the work of Bates et al. (Bates et al., 2017), the authors attempted to validate their simulation methods with different imaging conditions, by changing for example b-value and diffusion time. They simulated DTI at a voxel of size 200 μm^3 and validated the simulation using the averaged DW signal of a whole rat heart acquired

with isotropic resolution of 200 μm. They also demonstrated the effects of myocardium structures and diffusivity in intra-cellular space on diffusion metrics through a sensitivity analysis, and found that cross sectional area and diffusivity in intra-cellular space influence greatly the eigenvalues of diffusion tensor, but that the effect of myocyte volume fraction is negligible. This is the first work validating cardiac Monte Carlo random walk simulations with real acquisitions. However, validating with the averaged signal of whole heart may introduce bias and miss some interesting findings, such as local-related differences between simulations and acquisitions. In addition, the effects of microstructure were not fully considered in their work, like orientation disarray and diffusivity in extra-cellular space.

Our work solved the above-mentioned problems in cardiac DTI simulation. With the help of real DTI acquisitions of the same heart, we ~~can refine~~ the modeling and simulation parameters to make sure that the simulation results are more realistic. After that, ~~the detailed~~ analysis about the influence of microstructure variations on diffusion metrics allow us to explore underlying microstructures from macroscopic diffusion metrics. For instance, by comparing simulations and real acquisitions, we inferred that heart 2 has a larger mean myocyte diameter, a smaller gap between myocytes, a smaller orientation heterogeneity and a smaller intracellular diffusivity than the other hearts, which suggests that the properties of myocyte structure are related to the maturational change from the point of view of DTI. The established relationship between microscopic structure variations and macroscopic measurements in cardiac DTI could help in investigating some cardiac diseases.

However, there are still several limitations for this work. Firstly, although considered as gold-standard technique, PLI is a destructive fiber orientation imaging method. The image provided by PLI is not really a 3D volume (with slice spacing), which may cause that the fiber orientations provided by PLI do not match exactly any slices provided by DTI. In addition, real DTI acquisitions are noisy. Although we have improved the SNR by averaging the images acquired from multiple repetitions, the influence of noise on diffusion metrics still exists. These factors may cause the biases in inferring the underlying microstructures. Secondly, the geometrical models of myocardium were constructed from PLI, which, although able to provide myocyte orientations of a whole heart with a high spatial resolution, do not offer real morphological characteristics of myocytes. It has been verified that the substrate shape will influence simulation accuracy (Lee et al., 2020b). Therefore, incorporating true geometrical shapes of myocytes into our model for simulation would be a future work. Thirdly, all the simulations and acquisitions being performed on infant hearts, investigating the difference in modeling and simulation parameters on human adult hearts will help us further understand the longitudinal myocardium structure development using DTI. However, PLI acquisition ~~for~~ whole human adult hearts is technically very challenging, which prevents us from using the proposed method to explore the difference in microstructures between infant and adult hearts. Fourthly, as mentioned above, in this work we used DBR method to deal with the collision for saving computational time, but such method suffers from a bias in diffusion signals. Although the bias is acceptable but still influences slightly several analyses, such as convergence (Fig. 5 and Fig. A5) and correlation between diameter and λ_1 . Finally, this work focused on *ex vivo* hearts. Investigating the relationship between DTI diffusion metrics and *in vivo* myocardium structures is still a clinical challenge, since myocyte deformation and myocyte arrangement variation during a cardiac cycle remain unclear. An interesting future work would be to construct a realistic *in vivo* myocardium model to simulate the corresponding cardiac DTI with *in vivo* imaging sequences, such as the STEAM and M2-SE.

5. Conclusion

To get a realistic cardiac DTI simulation, the myocardium model of whole human heart was firstly constructed based on physical measurements of high-resolution PLI. Then the corresponding DTI was simulated with Block equation and Monte Carlo random walking methods. Finally, the modeling and simulation parameters were refined by matching the simulated DTI metrics and

the corresponding real acquisitions. The proposed simulation method enabled us to get insights into the effects of myocardial microstructure variations on DTI diffusion metrics. An increase of ECV was found to decrease FA and increase λ_1 and λ_2. The increase of orientation heterogeneity resulted in the decrease of FA and λ_1 but the increase of λ_2. Increasing myocyte diameter led to a higher λ_2 and a lower FA. As to the helix angle, the variations of ECV, orientation heterogeneity, and myocyte diameter can effect ~~the~~ estimation accuracy ~~of helix angle~~, especially for heterogeneity and ECV. In the future, the proposed DTI simulation method may be further used to investigate the influence of imaging sequence parameters on diffusion metrics and validate the corresponding mappings between DTI and microstructures.

Acknowledgments

The authors would like to thank Pierre Croisille and M. Viallon from University of Lyon and Yves USSON, Gabrielle MICHALOWICZ and Pierre-Simon JOUK from University Grenoble-Alpes for their DTI and PLI data acquisitions. This work is funded partially by the National Nature Science Foundations of China (Grant No.6216010271, 61661010, 61701105), the Guizhou Provincial Scientific Research Project ZK[2021]key 002, the National Key R&D Plan of China under Grant 2017YFB1400100, the Program PHC-Cai Yuanpei 2018 (No.41400TC), the International Research Project METISLAB, and the Committee of Science and Technology of Shanghai (No.19510711200).

References

Abdullah, O.M., Seidel, T., Dahl, M.J., Gomez, A.D., Yiep, G., Cortino, J., Sachse, F.B., Albertine, K.H., Hsu, E.W., 2016. Diffusion tensor imaging and histology of developing hearts. NMR in Biomedicine 29, 1338–1349.

Aliev, M.K., Dos Santos, P., Hoerter, J.A., Soboll, S., Tikhonov, A.N., Saks, V.A., 2002. Water content and its intracellular distribution in intact and saline perfused rat hearts revisited. Cardiovascular research 53, 48–58.

Andrews, S.S., Addy, N.J., Brent, R., Arkin, A.P., 2010. Detailed simulations of cell biology with Smoldyn 2.1. PLoS Computational Biology 6, e1000705.

Ariga, R., Tunnicliffe, E.M., Manohar, S.G., Mahmod, M., Raman, B., Piechnik, S.K., Francis, J.M., Robson, M.D., Neubauer, S., Watkins, H., 2019. Identification of Myocardial Disarray in Patients With Hypertrophic Cardiomyopathy and Ventricular Arrhythmias. Journal of the American College of Cardiology 73, 2493–2502.

Axel, L., Wedeen, V.J., Ennis, D.B., 2014. Probing dynamic myocardial microstructure with cardiac magnetic resonance diffusion tensor imaging. Journal of cardiovascular magnetic resonance : official journal of the Society for Cardiovascular Magnetic Resonance 16, 89.

Bates, J., Teh, I., McClymont, D., Kohl, P., Schneider, J.E., Grau, V., 2017. Monte Carlo Simulations of Diffusion Weighted MRI in Myocardium: Validation and Sensitivity Analysis. IEEE Transactions on Medical Imaging 36, 1316–1325.

Benson, A.P., Bernus, O., Dierckx, H., Gilbert, S.H., Greenwood, J.P., Holden, A.V., Mohee, K., Plein, S., Radjenovic, A., Ries, M.E., Smith, G.L., Sourbron, S., Walton, R.D., 2011. Construction and validation of anisotropic and orthotropic ventricular geometries for quantitative predictive cardiac electrophysiology. Interface focus 1, 101–116.

Berry, D.B., Regner, B., Galinsky, V., Ward, S.R., Frank, L.R., 2018. Relationships between tissue microstructure and the diffusion tensor in simulated skeletal muscle. Magnetic Resonance in Medicine 80, 317–329.

Brusini, L., Menegaz, G., Nilsson, M., 2019. Monte Carlo simulations of water exchange through myelin wraps: Implications for diffusion MRI. IEEE Transactions on Medical Imaging 38, 1438–1445.

Campbell, S.E., Gerdes, A.M., Smith, T.D., 1987. Comparison of Regional Differences in Cardiac Myocyte Dimensions in Rats, Hamsters, and Guinea Pigs 59, 53–59.

Carlson, R.V., Boyd, K.M., Webb, D.J., 2004. The revision of the declaration of helsinki: past, present and future. British journal of clinical pharmacology 57, 695–713.

Cook, A.C., Mohun, T.J., Oji, O., Garcia-canadilla, P., Schlossarek, S., Carrier, L., Mckenna, W.J., Moon, J.C., Captur, G., 2019. Myoarchitectural disarray of hypertrophic cardiomyopathy begins pre-birth. Journal of anatomy , 962–976.

Cook, P.A., Bai, Y., Nedjati-Gilani, S., Seunarine, K.K., Hall, M.G., Parker, G.J., Alexander, D.C., 2006. Camino: Open-source diffusion-MRI reconstruction and processing, in: 14th scientific meeting of the international society for magnetic resonance in medicine, p. 2759.

D. Streeter,, J., 1979. Gross Morphology and fiber geometry of the Heart. In Handbook of Physiology: The Cardiovascular System 1, 66–68.

Daducci, A., Canales-Rodríguez, E.J., Zhang, H., Dyrby, T.B., Alexander, D.C., Thiran, J.P., 2015. Accelerated Microstructure Imaging via Convex Optimization (AMICO) from diffusion MRI data. NeuroImage 105, 32–44.

Desrosiers, P.A., Michalowicz, G., Jouk, P., Usson, Y., Zhu, Y., 2016. Study of myocardial cell inhomogeneity of the human heart: Simulation and validation using polarized light imaging. Medical physics 43, 2273–2282.

Eriksson, T.S., Prassl, A.J., Plank, G., Holzapfel, G.A., 2013. Influence of myocardial fiber/sheet orientations on left ventricular mechanical contraction. Mathematics and Mechanics of Solids 18, 592–606.

Ferreira, P.F., Kilner, P.J., McGill, L.A., Nielles-Vallespin, S., Scott, A.D., Ho, S.Y., McCarthy, K.P., Haba, M.M., Ismail, T.F., Gatehouse, P.D., de Silva, R., Lyon, A.R., Prasad, S.K., Firmin, D.N., Pennell, D.J., 2014. In vivo cardiovascular magnetic resonance diffusion tensor imaging shows evidence of abnormal myocardial laminar orientations and mobility in hypertrophic cardiomyopathy. Journal of cardiovascular magnetic resonance : official journal of the Society for Cardiovascular Magnetic Resonance 16, 87.

Fick, R.H., Wassermann, D., Caruyer, E., Deriche, R., 2016. MAPL: Tissue microstructure estimation using Laplacian-regularized MAP-MRI and its application to HCP data. NeuroImage 134, 365–385.

Fieremans, E., Lee, H.H., 2018. Physical and numerical phantoms for the validation of brain microstructural mri: A cookbook. Neuroimage 182, 39–61.

Fieremans, E., Novikov, D., Sigmund, E., Liu, K., Jensen, J., Helpern, J., 2011. In vivo measurement of membrane permeability and fiber size in calf muscle using time-dependent dwi, in: Proc Intl Soc Mag Reson Med, p. 1153.

Gerdes, A.M., Kellerman, S.E., Moore, J.A., Muffly, K.E., Clark, L.C., Reaves, P.Y., Malec, K.B., McKeown, P.P., Schocken, D.D., 1992. Structural remodeling of cardiac myocytes in patients with ischemic cardiomyopathy. Circulation 86, 426–430.

Gerdes, A.M., Moore, J.O.A., Hines, J.M., Kirkland, P.A., Bishop, S.P., 1986. Regional Differences in Myocyte Size in Normal Rat Heart. The anatomical record. , 420–426.

Gilani, N., Malcolm, P., Johnson, G., 2017. A Monte Carlo Study of Restricted Diffusion: Implications for Diffusion MRI of Prostate Cancer. Magn Reson Med 77, 1671–1677.

Hall, M.G., Alexander, D.C., 2009. Convergence and parameter choice for monte-carlo simulations of diffusion mri. IEEE transactions on medical imaging 28, 1354–1364.

Helm, P., Beg, M.F., Miller, M.I., Winslow, R.L., 2005. Measuring and mapping cardiac fiber and laminar architecture using diffusion tensor MR imaging. Annals of the New York Academy of Sciences 1047, 296–307.

Helm, P.A., Younes, L., Beg, M.F., Ennis, D.B., Leclercq, C., Faris, O.P., McVeigh, E., Kass, D., Miller, M.I., Winslow, R.L., 2006. Evidence of structural remodeling in the dyssynchronous failing heart. Circulation Research 98, 125–132.

Hoyt, R.H., Cohen, M.L., Saffitz, J.E., 1989. Distribution and three-dimensional structure of intercellular junctions in canine myocardium. Circulation research 64, 563–574.

Hsu, E.W., Henriquez, C.S., 2001. Myocardial fiber orientation mapping using reduced encoding diffusion tensor imaging. Journal of cardiovascular magnetic resonance 3, 339–347.

Ianuş, A., Drobnjak, I., Alexander, D.C., 2016. Model-based estimation of microscopic anisotropy using diffusion mri: a simulation study. NMR in Biomedicine 29, 672–685.

Jouk, P.S., Mourad, A., Milisic, V., Michalowicz, G., Raoult, A., Caillerie, D., Usson, Y., 2007. Analysis of the fiber architecture of the heart by quantitative polarized light microscopy. Accuracy, limitations and contribution to the study of the fiber architecture of the ventricles during fetal and neonatal life. European journal of cardio-thoracic surgery 31, 915–921.

Jouk, P.S., Usson, Y., Michalowicz, G., Parazza, F., 1995. Mapping of the orientation of myocardial cells by means of polarized light and confocal scanning laser microscopy. Microscopy research and technique 30, 480–490.

Kerr, R.A., Bartol, T.M., Kaminsky, B., Dittrich, M., Chang, J.C.J., Baden, S.B., Sejnowski, T.J., Stiles, J.R., 2008. Fast Monte Carlo simulation methods for biological reaction-diffusion systems in solution and on surfaces. SIAM Journal on Scientific Computing 30, 3126–3149.

Khalique, Z., Pennell, D., 2019. Diffusion tensor cardiovascular magnetic resonance. Postgraduate medical journal 95, 433–438.

Kim, S., Chi-fishman, G., Barnett, A.S., Pierpaoli, C., 2005. Dependence on Diffusion Time of Apparent Diffusion Tensor of Ex Vivo Calf Tongue and Heart 1396, 1387–1396.

Kingsley, P.B., 2006. Introduction to Diffusion Tensor Imaging Mathematics : Part III . Tensor Calculation , Noise , Simulations , and optimization. Concepts in Magnetic Resonance Part A 28A, 155–179.

Kuchel, P.W., Durrant, C.J., 1999. Permeability Coefficients from NMR q-Space Data: Models with Unevenly Spaced Semi-permeable Parallel Membranes. Journal of Magnetic Resonance 139, 258–272.

Lee, H.H., Fieremans, E., Novikov, D.S., 2020a. Realistic microstructure simulator (rms): Monte carlo simulations of diffusion in three-dimensional cell segmentations of microscopy images. Journal of Neuroscience Methods 350, 109018.

Lee, H.H., Jespersen, S.N., Fieremans, E., Novikov, D.S., 2020b. The impact of realistic axonal shape on axon diameter estimation using diffusion mri. NeuroImage 223, 117228.

Lee, H.H., Papaioannou, A., Kim, S.L., Novikov, D.S., Fieremans, E., 2020c. A time-dependent diffusion mri signature of axon caliber variations and beading. Communications biology 3, 1–13.

Lee, H.H., Papaioannou, A., Novikov, D.S., Fieremans, E., 2020d. In vivo observation and biophysical interpretation of time-dependent diffusion in human cortical gray matter. NeuroImage 222, 117054.

Lombaert, H., Peyrat, J.M., Croisille, P., Rapacchi, S., Fanton, L., Cheriet, F., Clarysse, P., Magnin, I., Delingette, H., Ayache, N., 2012. Human atlas of the cardiac fiber architecture: study on a healthy population. IEEE transactions on medical imaging 31, 1436–1447.

McCain, M.L., Desplantez, T., Kléber, A.G., 2014. Engineering cardiac cell junctions in vitro to study the intercalated disc. Cell Communication and Adhesion 21, 181–191.

McGill, L.A., Scott, A.D., Ferreira, P.F., Nielles-Vallespin, S., Ismail, T., Kilner, P.J., Gatehouse, P.D., De Silva, R., Prasad, S.K., Giannakidis, A., Firmin, D.N., Pennell, D.J., 2015. Heterogeneity of fractional anisotropy and mean diffusivity measurements by in vivo diffusion tensor imaging in normal human hearts. PLoS ONE 10, e0132360.

Mekkaoui, C., Jackowski, M.P., Kostis, W.J., Stoeck, C.T., Thiagalingam, A., Reese, T.G., Reddy, V.Y., Ruskin, J.N., Kozerke, S., Sosnovik, D.E., 2018. Myocardial scar delineation using diffusion tensor magnetic resonance tractography. Journal of the American Heart Association 7, e007834.

Mingasson, T., Duval, T., Stikov, N., Cohen-Adad, J., 2017. AxonPacking: An open-source software to simulate arrangements of axons in white matter. Frontiers in Neuroinformatics 11, 1–12.

Moulin, K., Croisille, P., Feiweier, T., Delattre, B.M., Wei, H., Robert, B., Beuf, O., Viallon, M., 2016. In vivo free-breathing DTI and IVIM of the whole human heart using a real-time slice-followed SE-EPI navigator-based sequence: A reproducibility study in healthy volunteers. Magnetic Resonance in Medicine 76, 70–82.

Nguyen, C., Fan, Z., Xie, Y., Pang, J., Speier, P., Bi, X., Kobashigawa, J., Li, D., 2016. In vivo diffusion-tensor MRI of the human heart on a 3 tesla clinical scanner: An optimized second order (M2) motion compensated diffusion-preparation approach. Magnetic Resonance in Medicine 76, 1354–1363.

Nguyen, C.T., Dawkins, J., Bi, X., Marbán, E., Li, D., 2018a. Diffusion Tensor Cardiac Magnetic Resonance Reveals Exosomes From Cardiosphere-Derived Cells Preserve Myocardial Fiber Architecture After Myocardial Infarction. JACC: Basic to Translational Science 3, 97–109.

Nguyen, K.V., Hernández-Garzón, E., Valette, J., 2018b. Efficient GPU-based Monte-Carlo simulation of diffusion in real astrocytes reconstructed from confocal microscopy. Journal of Magnetic Resonance 296, 188–199.

Nielles-Vallespin, S., Khalique, Z., Ferreira, P.F., de Silva, R., Scott, A.D., Kilner, P., McGill, L.A., Giannakidis, A., Gatehouse, P.D., Ennis, D., Aliotta, E., Al-Khalil, M., Kellman, P., Mazilu, D., Balaban, R.S., Firmin, D.N., Arai, A.E., Pennell, D.J., 2017. Assessment of Myocardial Microstructural Dynamics by In Vivo Diffusion Tensor Cardiac Magnetic Resonance. Journal of the American College of Cardiology 69.

Pervolaraki, E., Dachtler, J., Anderson, R.A., Holden, A.V., 2017. Ventricular myocardium development and the role of connexins in the human fetal heart. Scientific Reports , 1–9URL: http://dx.doi.org/10.1038/s41598-017-11129-9.

Pluess, M., Daeubler, G., dos Remedios, C.G., Ehler, E., 2014. Adaptations of cytoarchitecture in human dilated cardiomyopathy. Biophysical Reviews 7, 25–32.

Poole-Wilson, P.A., 1995. The dimensions of human cardiac myocytes; confusion caused by methodology and pathology. Journal of Molecular and Cellular Cardiology 27, 863–865.

Rensonnet, G., Scherrer, B., Girard, G., Jankovski, A., Warfield, S.K., Macq, B., Thiran, J.P., Taquet, M., 2019. Towards microstructure fingerprinting: Estimation of tissue properties from a dictionary of Monte Carlo diffusion MRI simulations. NeuroImage 184, 964–980.

Rohr, S., 2004. Role of gap junctions in the propagation of the cardiac action potential. Cardiovascular Research 62, 309–322.

Rose, J.N., Nielles-Vallespin, S., Ferreira, P.F., Firmin, D.N., Scott, A.D., Doorly, D.J., 2019. Novel insights into in-vivo diffusion tensor cardiovascular magnetic resonance using computational modeling and a histology-based virtual microstructure. Magnetic Resonance in Medicine 81, 2759–2773.

Sapkota, N., Yoon, S., Thapa, B., Lee, Y.J., Bisson, E.F., Bowman, B.M., Miller, S.C., Shah, L.M., Rose, J.W., Jeong, E.K., 2016. Characterization of spinal cord white matter by suppressing signal from hindered space. A Monte Carlo simulation and an ex vivo ultrahigh-b diffusion-weighted imaging study. Journal of Magnetic Resonance 272, 53–59.

Scherrer, B., Schwartzman, A., Taquet, M., Sahin, M., Prabhu, S.P., Warfield, S.K., 2016. Characterizing brain tissue by assessment of the distribution of anisotropic microstructural environments in diffusion-compartment imaging (DIAMOND). Magnetic Resonance in Medicine 76, 963–977.

Scollan, D.F., Holmes, A., Winslow, R., Forder, J., 1998. Histological validation of myocardial microstructure obtained from diffusion tensor magnetic resonance imaging. The American journal of physiology 275, H2308–2318.

Scott, A.D., Nielles-vallespin, S., Ferreira, P.F., Khalique, Z., Gatehouse, P.D., Kilner, P., Pennell, D.J., Firmin, D.N., 2018. An in-vivo comparison of stimulated-echo and motion compensated spin-echo sequences for 3 T diffusion tensor cardiovascular magnetic resonance at multiple cardiac phases. Journal of cardiovascular magnetic resonance 20, 1–15.

Spach, M.S., Heidlage, J.F., Dolber, P.C., Barr, R.C., 1998. Extracellular discontinuities in cardiac muscle evidence for capillary effects on the action potential foot. Circulation Research 83, 1144–1164.

Stanisz, G.J., Odrobina, E.E., Pun, J., Escaravage, M., Graham, S.J., Bronskill, M.J., Henkelman, R.M., 2005. T1, T2 relaxation and magnetization transfer in tissue at 3T. Magnetic resonance in medicine 54, 507–12.

Strijkers, G.J., Bouts, A., Blankesteijn, W.M., Peeters, T.H.J.M., Vilanova, A., van Prooijen, M.C., Sanders, H.M.H.F., Heijman, E., Nicolay, K., 2009. Diffusion tensor imaging of left ventricular remodeling in response to myocardial infarction in the mouse. NMR in biomedicine 22, 182–90.

Tariq, M., Schneider, T., Alexander, D.C., Gandini Wheeler-Kingshott, C.A., Zhang, H., 2016. Bingham-NODDI: Mapping anisotropic orientation dispersion of neurites using diffusion MRI. NeuroImage 133, 207–223.

Toussaint, N., Stoeck, C.T., Sermesant, M., Schaeffter, T., Kozerke, S., Batchelor, P.G., 2013. In Vivo Human Cardiac Fibre Architecture Estimation using Shape-based Diffusion Tensor Processing. Medical Image Analysis 17, 1243–1255.

Tseng, W.Y.I., Dou, J., Reese, T.G., Wedeen, V.J., 2006. Imaging myocardial fiber disarray and intramural strain hypokinesis in hypertrophic cardiomyopathy with MRI. Journal of magnetic resonance imaging : JMRI 23, 1–8.

Vangelderen, P., Despres, D., Vanzijl, P., Moonen, C., . Evaluation of restricted diffusion in cylinders. phosphocreatine in rabbit leg muscle. Journal of magnetic resonance, series B .

Von Deuster, C., Sammut, E., Asner, L., Nordsletten, D., Lamata, P., Stoeck, C.T., Kozerke, S., Razavi, R., 2016. Studying Dynamic Myofiber Aggregate Reorientation in Dilated Cardiomyopathy Using in Vivo Magnetic Resonance Diffusion Tensor Imaging. Circulation: Cardiovascular Imaging 9.

Von Deuster, C., Stoeck, C.T., Genet, M., Atkinson, D., Kozerke, S., 2016. Spin echo versus stimulated echo diffusion tensor imaging of the in vivo human heart. Magnetic Resonance in Medicine 76, 862–872.

Wah, K., Keller, K.A., 2003. Postnatal Anatomical and Functional Development of the Heart : A Species Comparison. Birth Defects Research (Part B) , 309–320doi:10.1002/bdrb.10034.

Wang, L., Zhu, Y., Li, H., Liu, W., Magnin, I.E., 2012. Multiscale modeling and simulation of the cardiac fiber architecture for DMRI. IEEE transactions on bio-medical engineering 59, 16–9.

Wei, H., Viallon, M., Delattre, B., Moulin, K., Yang, F., Croisille, P., Zhu, Y., 2015. Free-breathing diffusion tensor imaging and tractography of the human heart in healthy volunteers using wavelet-based image fusion. Medical Imaging, IEEE Transactions on 34, 306–316.

Welsh, C.L., Di Bella, E.V., Hsu, E.W., 2015. Higher-Order Motion-Compensation for in Vivo Cardiac Diffusion Tensor Imaging in Rats. IEEE Transactions on Medical Imaging 34, 1843–1853.

Wu, E.X., Wu, Y., Tang, H., Wang, J., Yang, J., Ng, M.C., Yang, E.S., Chan, C.W., Zhu, S., Lau, C.P., Tse, H.F., 2007. Study of myocardial fiber pathway using magnetic resonance diffusion tensor imaging. Magnetic resonance imaging 25, 1048–1057.

Wu, R., An, D.A., Hu, J., Jiang, M., Guo, Q., Xu, J.R., Wu, L.M., 2018. The apparent diffusion coefficient is strongly correlated with extracellular volume, a measure of myocardial fibrosis, and subclinical cardiomyopathy in patients with systemic lupus erythematosus. Acta Radiologica 59, 287–295.

Xing, H., Lin, F., Wu, Q., Gong, Q., 2013. Investigation of different boundary treatment methods in monte-carlo simulations of diffusion nmr. Magnetic resonance in medicine 70, 1167–1172.

Yang, F., Zhu, Y.M., Michalowicz, G., Jouk, P.S., Fanton, L., Viallon, M., Clarysse, P., Croisille, P., Usson, Y., 2018. Quantitative comparison of human myocardial fiber orientations derived from DTI and polarized light imaging. Physics in Medicine and Biology 63, 11–14.

Yeh, C.h., 2011. Diffusion Microscopist Simulator-The Development and Application of a Monte Carlo Simulation System for Diffusion MRI. Ph.D. thesis. Universite Paris-Sud XI.

Yeh, C.H., Schmitt, B., Le Bihan, D., Li-Schlittgen, J.R., Lin, C.P., Poupon, C., 2013. Diffusion microscopist simulator: a general Monte Carlo simulation system for diffusion magnetic resonance imaging. PloS one 8, e76626.

Appendix

Variations of diffusion metric maps including FA, λ_1, λ_2, helix angle and error in helix angle with respect to ECV are given in Fig. A1.

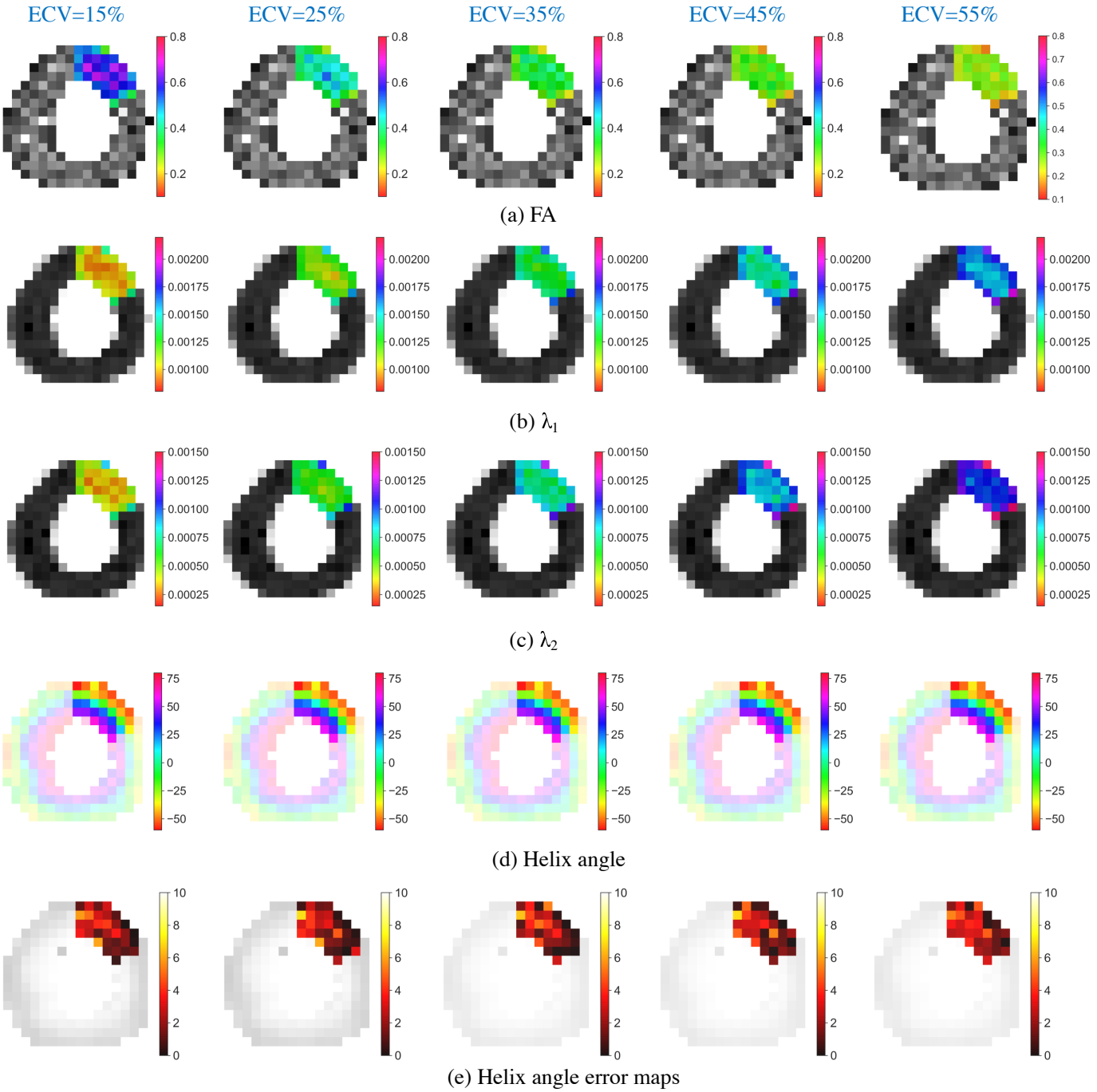

Fig. A1. Effects of ECV ratio on diffusion metrics. The other modeling parameters are: mean diameter is 8 μm, orientation heterogeneity is 0 °, myocyte length varies from 40-100 μm.

Variations of diffusion metric maps including FA, λ_1, λ_2, helix angle and error in helix angle with respect to orientation heterogeneity are given in Fig. A2.

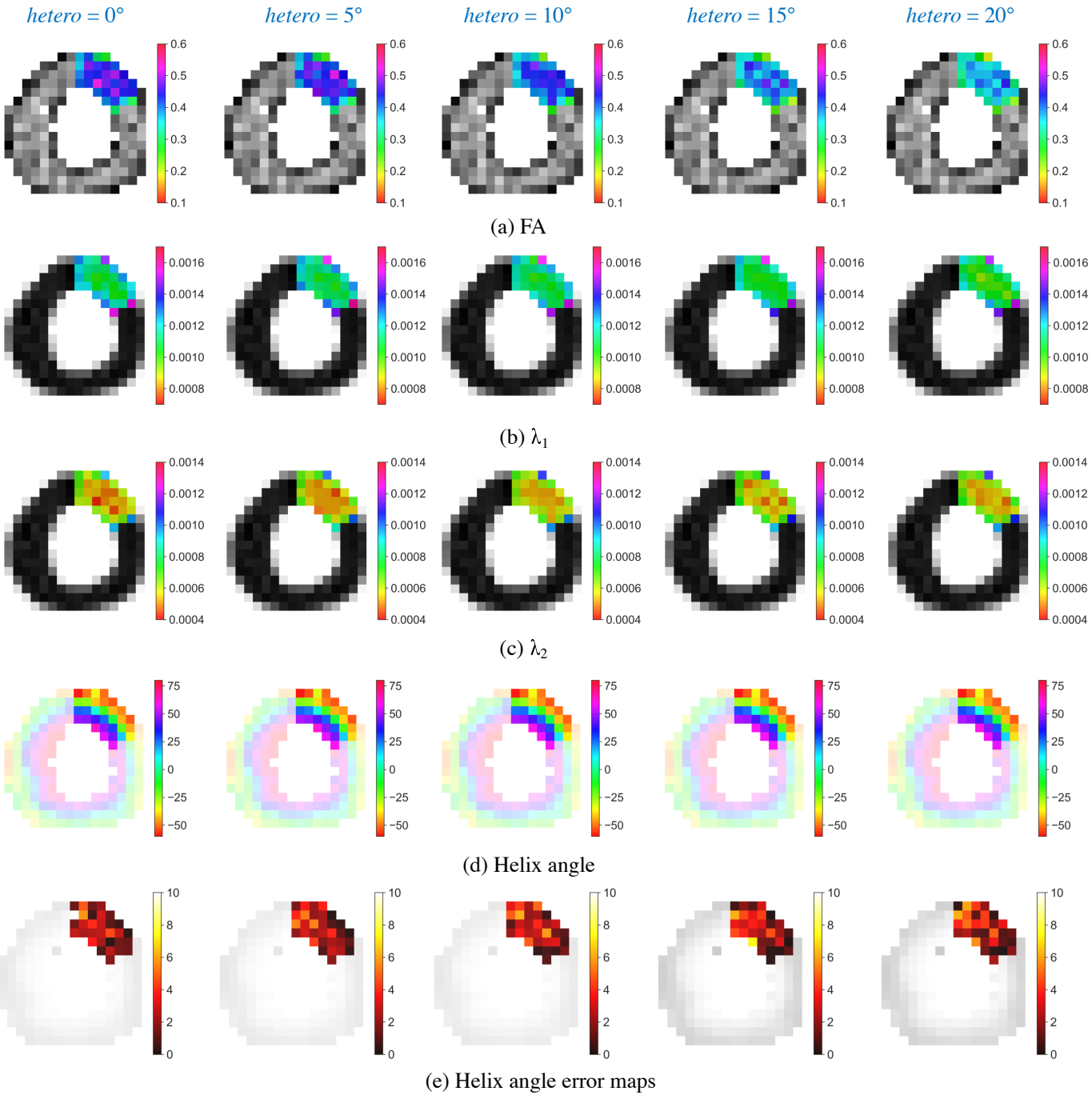

Fig. A2. Effects of orientation heterogeneity on diffusion metrics. The other modeling parameters are: mean diameter is 8 μm, the maximum gap between myoctes is 1 μm, and myocyte length varies from 40-100 μm. Note that the orientation heterogeneity here indicates the maximum angle that the fiber orientation rotated around itself.

Variations of diffusion metric maps including FA, λ_1, λ_2, helix angle and error in helix angle with respect to myocyte diameter are given in Fig. A3.

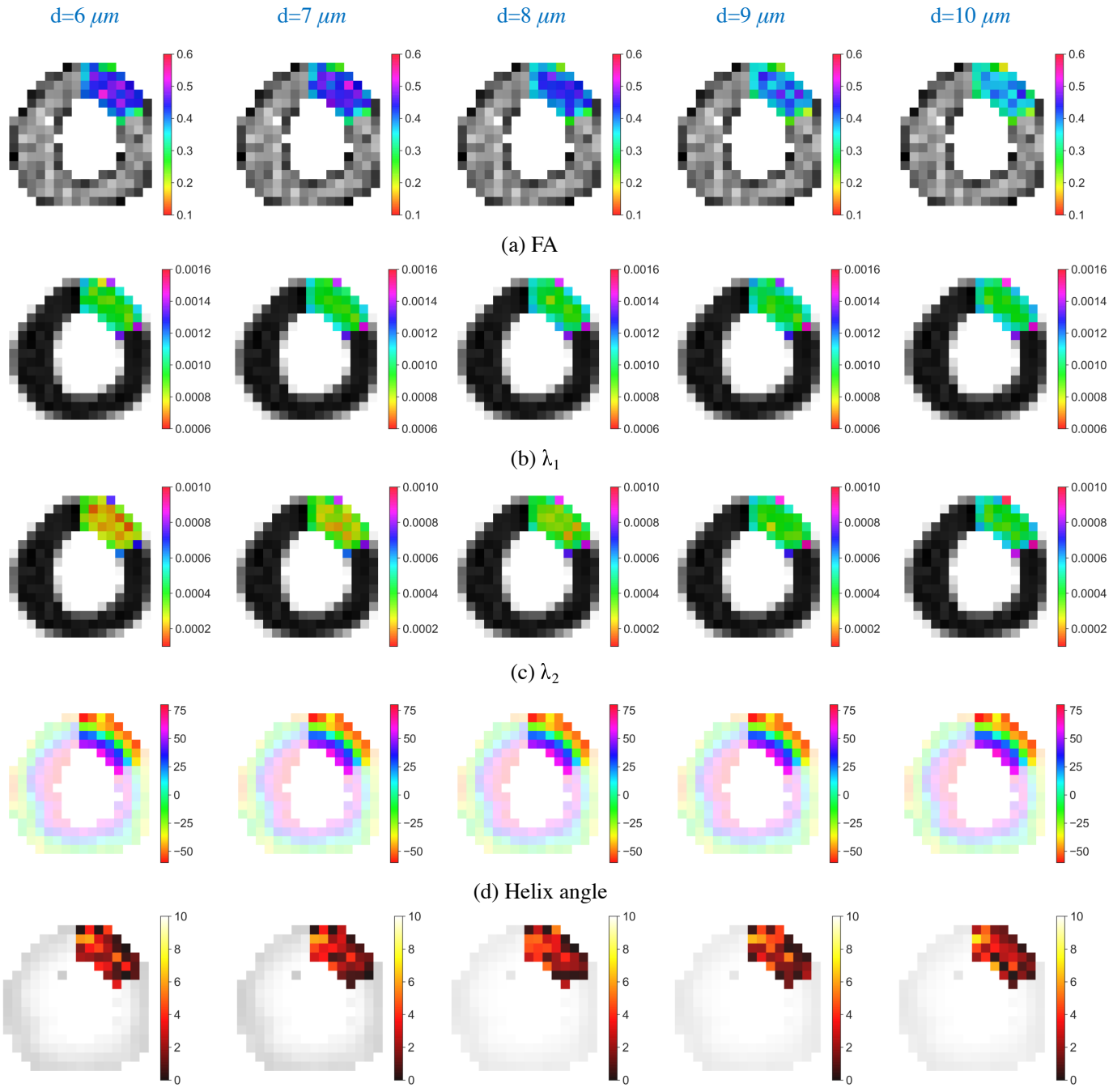

Fig. A3. Effects of myocyte diameter on diffusion metrics. The other modeling parameters are: orientation heterogeneity is 0 °, maximum gap between myoctes is 0 μm, and myocyte length varies from 40-100 μm.

In the manuscript, we only showed the convergence result obtained with different number of particles while fixing the number of steps as 10000. To fully understand the influence of the number of particles and steps, in Fig. A4, are provided the variations in RMAE of diffusion signals as a function of the number of particles for different number of steps. We observe that when the number of particles is more than 5000, RMAE decreases with the increase of number of steps. By Varying the number of steps from 100 to 10000, RMAE decreases by about 0.4% at most.

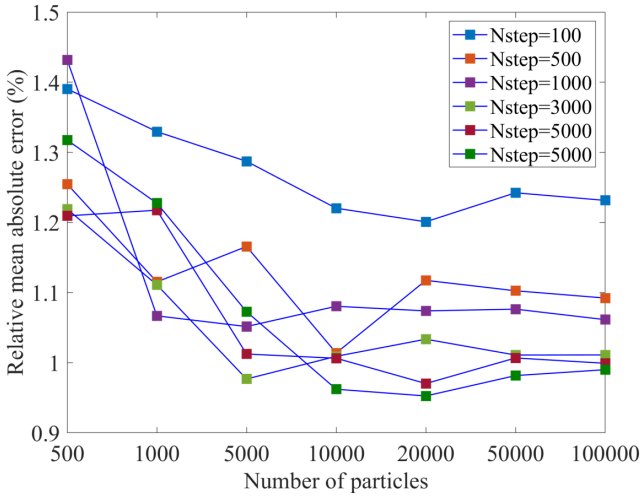

Fig. A4. The variations of RMAE of diffusion signal with the number of particles obtained with different number of steps.

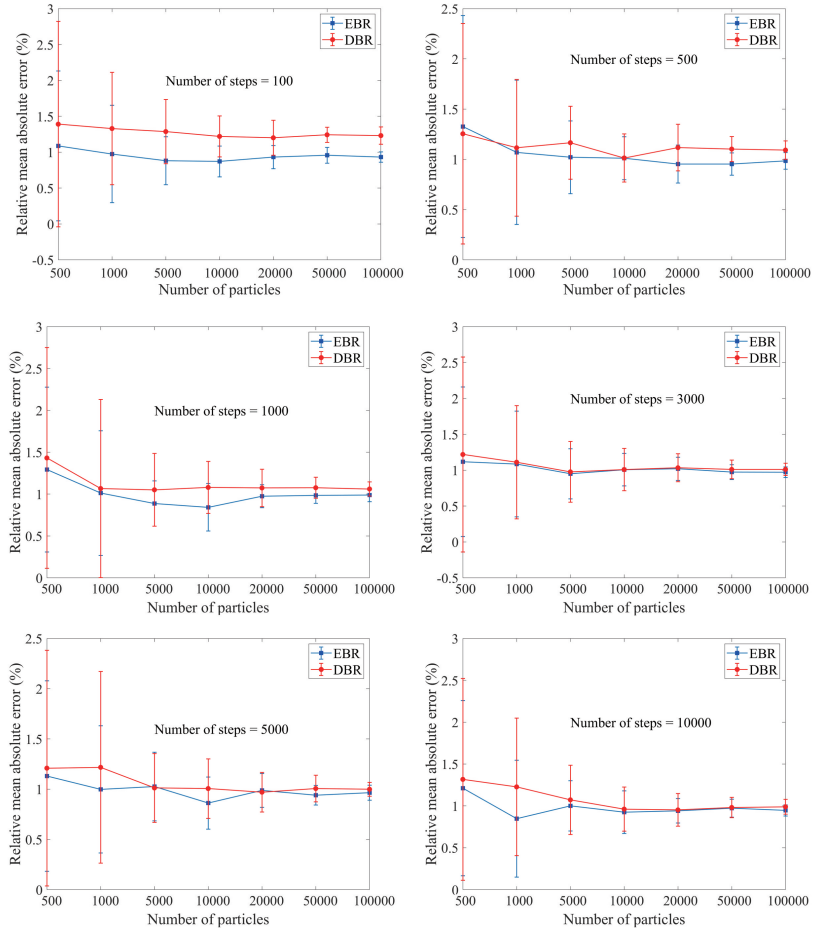

Fig. A5. The difference in RMAE between EBR and DBR obtained with different numbers of particles and steps.

The difference between EBR (elastic boundary reflection) and DBR (diffuse boundary reflection) obtained with different numbers of steps and particles is ~~given~~ in Fig. A5. As the number of steps is larger than 1000 and the number of particles is more than 10000, there is almost no significant difference between EBR and DBR.